Harnessing cell-encapsulated hydrogels to study astrocyte mechanoresponse in 4D

Ana N. Strat[a,b,c], Suhani Patel[a], Minh-Tri Ho Thanh[c,d], Alexander Kirschner[a], Souvik Ghosh[a,c], Michael P. Geiss[c,d], Mariano Viapiano[b], Yutao Liu[e], Alison E. Patteson[c,d], Samuel Herberg[a,c,e,f,g,h], Preethi S. Ganapathy[a,b,c]

Affiliations:

[a]Department of Ophthalmology & Visual Sciences, SUNY Upstate Medical University, Syracuse, NY 13210, USA

[b]Department of Neuroscience and Physiology, SUNY Upstate Medical University, Syracuse, NY 13210, USA

[c]BioInspired Institute, Syracuse University, Syracuse, NY 13244, USA

[d]Department of Physics, Syracuse University, Syracuse, NY 13244, USA

[e]Department of Cellular Biology and Anatomy, Augusta University, Augusta, GA 30912 , USA

[f]Department of Cell and Developmental Biology, SUNY Upstate Medical University, Syracuse, NY 13210, USA

[g]Department of Biochemistry and Molecular Biology, SUNY Upstate Medical University, Syracuse, NY 13210, USA

[h]Department of Biomedical and Chemical Engineering, Syracuse University, Syracuse, NY 13244, USA

*To whom correspondence should be addressed: Preethi S. Ganapathy MD, PhD; Assistant Professor; Department of Ophthalmology & Visual Sciences, SUNY Upstate Medical University, 505 Irving Avenue, Neuroscience Research Building Room 4606, Syracuse, NY 13210, USA, email: ganapatp@upstate.edu

Keywords: optic nerve head astrocytes, biomechanical strain, glaucoma, mechanobiology, ECM hydrogels, transcriptomics, morphology

Abbreviations

ATP adenosine triphosphate
ATR ataxia telangiectasia and Rad3 related
CNS central nervous system
ECM extracellular matrix
ETC electron transport chain
F-actin filamentous actin
GFAP glial fibrillary acidic protein
HIF-1α hypoxia-inducible factor 1 α
IL6 interleukin 6
IL17 interleukin 17
IOP intraocular pressure
MONHA mouse optic nerve head astrocyte
mTOR mammalian target of rapamycin
ONH optic nerve head
PI3K-Akt phosphoinositide 3-kinase Ak strain transforming
TGFβ2 transforming growth factor beta 2

Abstract

In glaucoma, the optic nerve head (ONH) is exposed to increased biomechanical strain, impacting the resident astrocytes that maintain neural homeostasis. After injury, astrocytes exhibit morphologic and metabolic shifts; however, the specific impact of glaucoma-related biomechanical strains on astrocyte behavior remains poorly understood. To address this, we utilized our previously established 3D cell-encapsulated ECM hydrogel to elucidate ONH astrocyte transcriptomic and cellular responses to varying biomechanical strain levels over time. Murine ONH astrocyte-encapsulated hydrogels were subjected to 0, 3, or 10% cyclic strain for 4h and 24h. Using confocal reflectance microscopy, we observed that hydrogel porosity was adequate for nutrient supplementation, while bulk hydrogel stiffness and cell viability remained unchanged after biomechanical strain. Mechanotranscriptional responses were robustly altered within 4h in a hydrogel region-, strain-, and time-dependent manner. RNA sequencing revealed changes in gene expression related to cell morphology, division, senescence, hypoxia, metabolism, and ECM regulation. Morphometric analyses of strained ONH astrocytes showed reduced F-actin area coverage, increased GFAP, HIF-1α, fibronectin, and collagen fibril reorganization. Our findings demonstrate that ONH astrocyte transcriptional responses are highly dependent on duration/magnitude of biomechanical strain and surrounding ECM density, corresponding with altered cell morphology, hypoxia, and ECM modification. This ONH astrocyte-encapsulated hydrogel provides a valuable platform for nuanced future manipulation of porosity, ECM composition, and cellularity to study the impact of biomechanical strain on ONH pathophysiology.

113 ***1. Introduction***

114 Astrocytes are the master glial cells regulating central nervous system (CNS) homeostasis.
115 They provide trophic and matrix support to neurons, contribute to modulating synaptic activity
116 and interact with neighboring glial cells and blood vessels to ensure optimal function and
117 protection of neuronal tissue [1-5]. Astrocytes are highly sensitive to biomechanical stimuli, with
118 their development and heterogeneity influenced by the surrounding biomechanical environment
119 [6-8]. Equally important to healthy physiologic conditions is the response of astrocytes to different
120 biomechanical insults within a diseased CNS. In neuropathies induced acutely by trauma (i.e.,
121 traumatic brain or spinal cord injuries) or chronically by neurodegeneration (i.e., glioblastoma or
122 glaucoma), astrocytes are subjected to various degrees of pathological biomechanical stimuli -
123 compression, tension, tissue stiffening/softening - and their mechanoresponse is directed by the
124 magnitude and duration of these cues [9-11].

125 One of the hallmark features of astrocyte response to pathological biomechanical stimuli
126 is the development of reactive astrogliosis [4, 12-15]. In glaucoma, this phenomenon is most
127 notable within the optic nerve head (ONH), where there is progressive loss of retinal ganglion cells
128 ultimately leading to irreversible blindness [16, 17]. The local astrocytes within this region
129 provide key support to axons and are first responders to acute glaucomatous insult prior to neuronal
130 dysfunction [18, 19]. As part of their early response, astrocytes lose their stellate morphology in
131 favor of a more polarized cell shape; they also drastically alter their actin cytoskeleton architecture,
132 and upregulate intermediate filament proteins associated with reactive gliosis such as glial
133 fibrillary acidic protein (GFAP), vimentin, and nestin [18, 20-23].

134 As the disease progresses, astrocytes decouple from neighboring cells and remodel the
135 surrounding extracellular matrix (ECM) by significantly increasing production of ECM proteins

136 (i.e., fibronectin and collagen IV), matrix crosslinking/degrading enzymes (i.e., transglutaminase
137 2 and matrix metalloproteinases 2/9), and pro-fibrotic cytokines (i.e., transforming growth factor
138 beta 2 (TGFβ2)) [24-26]. These glial cells are also responsible for matching the metabolic demand
139 of neurons under stress. This metabolic interdependence, exemplified by the glutamate-glutamine
140 cycle and astrocyte-mediated vasodilation, is crucial for neuronal health and its disruption
141 contributes to neurodegenerative diseases [5, 27].

142 Evidence supports that the ONH in glaucoma is subjected to various degrees of
143 compressive and tensile strains that vary by microregion. Specifically, finite element modeling
144 studies predict between 3-10% compressive and 2-5% tensile biomechanical strain on the ONH
145 with intraocular pressure (IOP) elevation [28-30]. While many studies have used such modeling
146 approaches to understand the biomechanical strains within the glaucomatous ONH, there are
147 limited reports on the direct transcriptional and morphologic response of local astrocytes to
148 isolated biomechanical strains. This is a crucial gap in our understanding of how glaucomatous
149 biomechanical strains can impact astrocyte behavior and, ultimately, disrupt their functional
150 support of neurons. Prior studies have reported on ONH astrocyte cell cultures subjected to
151 mechanical stressors such as hydrostatic pressure and tension in 2D [27, 31, 32]. While not without
152 merit, conventional 2D *in vitro* culture systems are not suitable to analyze 3D astrocyte
153 morphological complexity and coupling under biomechanical forces. Furthermore, it is nearly
154 impossible to subject monolayer astrocyte cultures to compression in 2D.

155 We previously developed a cell-encapsulated hydrogel system containing murine ONH
156 astrocytes and ECM biopolymers (collagen type I and hyaluronic acid), which permits detailed
157 analysis of cell shape and cell-cell/cell-ECM interactions in 3D [33]. In the present study, we
158 investigated how ONH astrocytes that are encapsulated within this ECM hydrogel respond to

159 varying degrees of compressive biomechanical strain over time (i.e., in 4D) using a well-
160 established bioreactor [34-36]. We aimed to thoroughly characterize the transcriptional and
161 morphological responses of astrocytes to strain magnitude and duration, and ECM collagen
162 density. To achieve this, we conducted bulk RNA sequencing and morphometric analyses to
163 determine changes in gene expression, cytoskeletal organization, metabolic function and ECM
164 remodeling over time. Ultimately, our study represents a comprehensive investigation of time-
165 dependent ONH astrocyte mechanoresponses to glaucoma-relevant biomechanical strains and
166 seeks to provide mechanistic insights into broader astrocyte mechanodysfunction in
167 neurodegenerative diseases of the CNS.
168

169 ## *2. Methods*

170 ### *2.1 Mouse ONH astrocyte isolation and culture*

171 C57BL/6J mice were purchased from the Jackson Laboratory (Bar Harbor, ME) and bred
172 in house according to the institutional guidelines for the humane treatment of animals (IACUC
173 #473) and to the ARVO Statement for the Use of Animals in Ophthalmic and Vision Research.
174 Each harvest used 5-8 mice aged 6-8 weeks. The isolation/culture of primary mouse ONH
175 astrocytes (MONHAs) was performed as previously described [37]. Briefly, optic nerve head
176 tissue was dissected from each eye using a SMZ1270 stereomicroscope at a location proximal to
177 the sclera. The samples then underwent digestion in 0.25% trypsin (Invitrogen, 25200-056,
178 Carlsbad, CA, USA) for 15 minutes at 37 °C. Following digestion, the tissue was resuspended in
179 MONHA growth medium, consisting of Dulbecco's modified Eagle's medium, DMEM/F12
180 (Invitrogen, 11330-032, Grand Island, NE, USA), supplemented with 10% fetal bovine serum
181 (FBS; Atlanta Biologicals, S11550, Atlanta, GA, USA), 1% penicillin/streptomycin (Corning, 30-

182 001-CI, Manassas, VA, USA), 1% Glutamax (Invitrogen, 35050-061, Grand Island, NY, USA),
183 and 25 ng/ml epidermal growth factor (EGF; Sigma, E4127-5X, St. Louis, MO, USA). The
184 digested ONH tissue was then plated onto T75 cell culture flasks coated with 0.2% gelatin and
185 incubated at 37 °C in a humidified atmosphere with 5% CO2. MONHAs migrated from the ONH
186 tissue over a period of 10-14 days before the first passage. All subsequent experiments included
187 MONHAs at passage 3.

188 ***2.2 Preparation of PDMS molds***

189 A polydimethylsiloxane (PDMS) mixture was used at a 10:1 ratio of elastomer to curing
190 agent as per the manufacturer's instructions (PDMS; Sylgard 184, Dow Corning, Midland, MI,
191 USA). This mixture was poured into custom 3D printed ABS-M30 filament negative molds (F170;
192 Stratasys, Eden Prairie, MN, USA), measuring either 10 mm diameter x 6 mm depth or 8 mm
193 diameter x 4 mm depth, cured at 60°C, and autoclaved prior to use.

194 ***2.3 Preparation of MONHA-encapsulated hydrogels***

195 MONHA-encapsulated hydrogels were prepared as previously described [33]. Briefly,
196 MONHAs (2.5×10^6 cells/ml) in media were mixed with 3.1 mg/ml methacrylate-conjugated
197 bovine collagen type I (MA-COL; molecular weight: ~300 kDa, degree of methacrylation: ~60–
198 70%; Advanced BioMatrix, Carlsbad, CA, USA), 1 mg/ml thiol-conjugated hyaluronic acid (SH-
199 HA; Glycosil®; molecular weight: ~300 kDa, degree of thiolation: ~20–30%; Advanced
200 BioMatrix), and 0.025% (w/v) riboflavin (Sigma-Aldrich, R7774, Darmstadt, Germany)
201 (photoinitiator) on ice. The chilled MONHA hydrogel precursor solution was pipetted as 250 µl
202 into 8 x 4 mm PDMS molds or 500 µl into 10 x 6 mm PDMS molds. Constructs were then
203 crosslinked by exposure to low intensity blue light (405-500 nm) (OmniCure S1500 UV Spot
204 Curing System; Excelitas Technologies, Mississauga, Ontario, Canada) at 10.3 mW/cm^2 intensity

205 for 5 minutes. Following hydrogel crosslinking, each MONHA-encapsulated hydrogel was
206 carefully removed from its respective PDMS mold and left in MONHA growth medium [33, 37].
207 MONHA-hydrogels were cultured for 14 days prior to any experiments, and media was
208 replenished every 2-3 days.

209 ***2.4 MONHA-encapsulated hydrogel pore size analysis***

210 The collagen network of acellular and MONHA-encapsulated hydrogels was imaged with
211 confocal reflectance microscopy on a Zeiss LSM980 scanning confocal microscope (Carl Zeiss
212 Microscopy, Jena, Germany) using a 40x water immersion objective (LD LCI Plan-Apochromat
213 40x/1.2 Imm Corr DIC M27, Zeiss). The excitation wavelength was set to 488 nm and backscatter
214 signal was collected via a beam splitter BC80/20. Pore size within the collagen gel was calculated
215 using an algorithm as previously described [38]. In brief, 6-9 fields of view were obtained from
216 the core and periphery of MONHA-encapsulated hydrogels for each magnitude of strain (i.e., 0%,
217 3%, or 10%) at each timepoint (i.e., 4 hours, 24 hours). The image size was set to 1024 x 1024
218 pixels in x/y and the z-step interval set to 0.5 μm collecting a total of 50 μm in the z-axis direction.
219 The confocal z-stack images of the collagen gel were input to FIbeR Extraction MATLAB code
220 [39] to extract the Euclidean distance map. The pore size was then extracted using the bubble
221 analysis algorithm in MATLAB [40].

222 ***2.5 MONHA-encapsulated hydrogel permeability analysis***

223 To determine the permeability of MONHA-encapsulated hydrogels, acellular and
224 MONHA-encapsulated hydrogels were crosslinked on top of 3 μm pore size transwell inserts in
225 12-well plates (Thermo Fisher, 141080, Kennebunk, Maine, USA). Before initiating the
226 permeabilization assay, gels were equilibrated in DMEM/F12 for 24h. The assay was initiated by
227 adding 200 μl of a 1000 μg/ml FITC-labelled dextran (70 kDa) tracer solution (FITC-DEAE-

228 Dextran; Sigma, 54702-1G) into the top chamber above each hydrogel. In the bottom chamber,
229 1000 µl Dulbecco's Phosphate Buffered Saline 1X (DPBS; Invitrogen, 14190-44) was added
230 which served as receiving medium. The tracer molecule leakage into the bottom well was
231 quantified (i.e., after permeating through the hydrogel). A volume of 600 µl from the bottom well
232 was withdrawn at each time point (5, 10, 15, 30, 45 min – 1, 2 h), and each time it was replenished
233 by an equal volume of fresh DPBS. For quantification, a standard curve was generated using
234 graded dilutions of FITC-labelled dextran (1 to 1000 µg/ml). A volume of 200 µL for each
235 supernatant sample and standard were transferred into a 96-well plate and absorbance was
236 measured at 490 nm using a BioTek Gen5 microplate reader (version 3.16; Agilent Technologies,
237 Palo Alto, CA, United States). The concentration of "leaked" FITC-labelled dextran in the
238 collected samples was determined using a standard curve equation and as previously described
239 [41, 42]. Cumulative FITC-labelled dextran at each time point was calculated by using:
240
241 Total FITC-labelled dextran in the bottom chamber before removal at time point t:$\text{Total}_t = C_t$
242 $\times 1000\mu L$;where C_t is concentration FITC-DEX at time point t.
243 Total FITC-DEX removed at time point t:$\text{Removed}_t(\mu g) = Ct \times 600\mu L$; where 600 μL= volume
244 removed.
245 Remaining FITC-DEX in the bottom well after removal at time point t:$\text{Remaining}_t\ (\mu g)=\text{Total}_t$
246 $(\mu g)-\text{Removed}_t\ (\mu g)$.
247 The cumulative leaked FITC-labelled dextran up to time point t :
248 $$\text{Cumulative}_t = \sum_{t=0}^{t} Removed_t\ (\mu g)$$
249

250 ***2.6 MONHA-encapsulated hydrogel collagen fiber signal intensity, compaction and cell***
251 ***alignment analysis***

252 For collagen signal intensity and compaction analyses, MONHA-encapsulated hydrogels
253 were imaged using confocal reflectance microscopy (see Methods 2.4). Fold-change collagen
254 signal intensity in MONHA-encapsulated hydrogels was quantified with background subtraction
255 from an acellular hydrogel using Z-project Maximum Intensity Projection in FIJI and further
256 normalized to number of nuclei. Collagen compaction was determined as previously described
257 [43]. In brief, the mean intensity of collagen fibrils in the fixed area around the astrocytes was
258 computed and then normalized against the mean intensity of the collagen fibrils as deduced from
259 acellular collagen images. The cropped area was found with binarized fluorescent images of the
260 astrocytes with pretrained denoising convolutional neural network (dsCNN)/median filter and
261 adaptive threshold functions in MATLAB. Moreover, due to the large sample size (number of
262 pixel intensity N > 10000), we used Cohen's effect size d to compare the relative difference
263 between the mean value of different groups (i.e., substantive significance), which scales with
264 sample size unlike p-value (i.e., statistical significance) [44]. Cohen's d = 0.20, 0.50, and 0.80 was
265 used to indicate the effect size as small, medium, or large, respectively.

266 ***2.7 Mechanical loading of MONHA-encapsulated hydrogels***

267 Using a custom bioreactor system [34-36], unconfined MONHA-encapsulated hydrogels
268 were cultured for 14 days, then subjected to either 0%, 3% or 10% cyclic compressive strain at
269 1Hz for 4 hours and 24 hours. These biomechanical strain intensities have been previously
270 correlated with strains within the glaucomatous ONH [28-30]. Hydrogels were placed on PDMS-
271 coated glass containers and maintained in 40 ml of astrocyte media for the duration of
272 biomechanical strain. A thermoplastic polyester platen attached to a linear actuator (Zaber Inc.,

273 NA08A30-T4), with 5 mm clearance from the glass wall and 10 perforations (5 mm in
274 diameter/perforation) cyclically compressed the hydrogels to 3 or 10% of their height. 0% static
275 controls were maintained in similar conditions with the platen immediately above the hydrogels,
276 but not actively compressing them. For post-strain analysis, the top 1 mm (adjacent to the
277 compressive platen) and bottom 1 mm (adjacent to the glass container) were discarded as to avoid
278 any biased effects caused by contact with the platen or glass container, and the 3 mm core was
279 further separated from the periphery of the hydrogel to allow for systematic comparisons between
280 different regions, magnitudes and durations of biomechanical strain.

281 ***2.8 MONHA-encapsulated hydrogel cell viability analyses***

282 Cell viability within the hydrogel was determined using a CellTiter 96® Aqueous Non-
283 Radioactive Cell Proliferation Assay (MTS; Promega, Madison, WI, USA) as per the
284 manufacturer's instructions. Following 24 hours of cyclic strain, MONHA-encapsulated hydrogels
285 were incubated with the staining solution (114 µl MTS, 6 µl PMS solution, 600 µl media) at 37 °C
286 for 4h, and absorbance at 490 nm was assessed with a spectrophotometer plate reader (BioTEK,
287 Winooski, VT, USA). Fold-change over time of blank-corrected absorbance values was analyzed
288 to quantify cell viability in hydrogels.

289 ***2.9 RNA sequencing and data sharing***

290 The 3 mm core and the remaining periphery of MONHA-encapsulated hydrogels were
291 isolated after biomechanical strain for bulk RNA-sequencing. Three samples per strain group (i.e.,
292 0%, 3%, 10%) at each time point (i.e., 4h, 24h) were used. Briefly, each sample was homogenized
293 for 2 minutes using a Fisherbrand™ 150 Handheld Homogenizer. Total RNA was extracted using
294 Trizol reagent (Invitrogen, 15596026, Carlsbad, CA, United States) according to the
295 manufacturer's protocol. 250 ng of extracted RNA was used as input to the Illumina Stranded

296 mRNA Library prep kit as per the manufacturer's instructions. Library quality and quantity was
297 assessed with Agilent 2100 Bioanalyzer (Agilent Technologies, Palo Alto, CA, United States). 36
298 libraries were pooled together for sequencing on an Illumina NextSeq 2000 next-generation
299 sequencing instrument with paired end 2x100bp. High-quality clean reads were filtered into
300 FASTQ format. RNA sequencing data is deposited and accessible through NIH Gene Expression
301 Omnibus (GEO) DataSets GSE300233.

302 ***2.10 Bioinformatic data analysis***

303 RNA-seq data were analysed using the online platform Illumina Partek-Flow (version
304 12.6.1) (Chesterfield, Missouri, USA). Briefly, FASTQ files were subjected to sequence quality
305 checks using "QC for Sequencing Reads" tool. Using the STAR 2.7.8a tool the reads were mapped
306 against the mouse reference genome mm39. Aligned reads were then quantified to annotation
307 model of mouse genome. Principal component analysis (PCA) of the top 2000 genes with greatest
308 variance in expression was applied to all samples to delineate clustered groups between
309 biomechanical strain durations and intensities. Differentially expressed genes (DEGs) across time
310 (i.e., 24h vs 4h) and biomechanical strain magnitude (i.e., 0% vs 3% vs 10%) as cofactors were
311 determined using ANOVA. Separately, pairwise comparisons between biomechanical strain
312 intensities (i.e., 3% vs 0%, and 10% vs 0%) at each timepoint (i.e., 4h or 24h) within each hydrogel
313 region (i.e., core or periphery) were identified using DESeq2 tool. For both analyses, the genes
314 and transcripts with FDR corrected p-value ≤ 0.05 and $|\text{Log2 fold change}| \geq 1.50$ were considered
315 differentially expressed. Gene ontology (GO) pertaining to biological process, cellular component,
316 and molecular function for each individual comparison was determined based on the over
317 representation analysis (ORA) using the publicly available enrichment tool WEB-based GEne SeT
318 AnaLysis Toolkit (https://www.webgestalt.org) [45, 46] with FDR corrected p-value ≤ 0.05. Gene

319 Set Enrichment Analysis (GSEA) against KEGG/Reactome databases was used to delineate altered
320 molecular pathways across time amongst all groups and significance was set to FDR corrected p-
321 value ≤ 0.05 and |Log2 fold change| ≥ 1.50.

322 ***2.11 Encapsulated MONHA morphological analysis***

323 Following application of biomechanical strain, MONHA-encapsulated hydrogels were
324 fixed with 4% PFA at 4 °C overnight, permeabilized with 0.5% Triton™ X-100 (Thermo Fisher
325 Scientific) and stained for filamentous actin (F-actin; Alexa Fluor® 488- or 594- conjugated
326 Phalloidin (1:200, Abcam, Ab176757 or Ab176753); nuclei were counterstained with DAPI.
327 Fluorescent z-stack images were captured using an air 20x objective (Plan-Apochromat 20x/0.8
328 M27, Zeiss) and a Zeiss LSM780 scanning confocal microscope (Carl Zeiss Microscopy, Jena,
329 Germany). The image size was set to 1024 x 1024 pixels or 512 x 512 in x/y, and six titled z-stack
330 images consisting of 100 µm in z-axis direction with the z-step interval set to 1.3 µm were obtained.
331 Assessment of cell morphology was conducted using Z-project Maximum Intensity Projection in
332 FIJI (NIH, Bethesda, MD) across individual z-stacks. F-actin masks were then generated and
333 binarized in FIJI, and the area of F-actin coverage was calculated by the ratio of percentage of
334 pixels with non-zero pixels [47].

335 ***2.12 MONHA-encapsulated hydrogel sectioning and immunohistochemical analysis***

336 MONHA-encapsulated hydrogels were cultured for 14 days prior to biomechanical loading
337 for 4h and 24h and then fixed with 1% Pagano fixative solution (i.e., 4% PFA, 50 mM Sucrose,
338 25 mM MgCl2, 2.5 mM KCl, HEPES 7.4) [48] at 4°C overnight. Samples were then washed with
339 DPBS and embedded in 10% bovine gelatin (Sigma-Aldrich, G9382-500G). Subsequently,
340 gelatin-embedded MONHA-encapsulated hydrogels were fixed again with 1% Pagano fixative
341 solution at 4°C overnight and then washed with DBPS. Using the Leica VT1000 S vibratome, 150

342 μm sections were cut and collected in cold PBS. Sections were then permeabilized with 0.5%
343 Triton™ X-100 for 15 min, blocked in 7% normal goat serum (Abcam, Ab7481) for 1h and
344 immunostained in 1% normal goat serum (Abcam, Ab7481) for either GFAP (Anti-GFAP
345 Antibody Cy3 Conjugate, 1:100, Millipore, MAB3402C3), fibronectin (rabbit anti-fibronectin
346 antibody, 1:100, Abcam, Ab2413) or hypoxia-inducible factor 1α (HIF-1α; rabbit anti-HIF-1
347 alpha antibody, 1:200, Abcam, Ab228649) overnight, followed by stain with Alexa Fluor® 488-
348 conjugated secondary antibody (goat polyclonal antibody to rabbit IgG, 1:500, Abcam, Ab150077)
349 for 1 h; nuclei were counterstained with DAPI (Abcam, Ab228549). Sections were mounted with
350 ProLong™ Gold Antifade (Thermo Fisher Scientific, P36930, Waltham, MA, USA) on
351 Superfrost™ Plus microscope slides (Fisher Scientific, 1255015). 3-4 fields of view per core or
352 periphery of the hydrogel were acquired using an air 40x objective (S Plan Fluor 40x/0.6, Nikon)
353 and an Andor BC43 SR spinning-disk confocal microscope (Oxford Instruments, Belfast, Northern
354 Ireland). The image size was set to 2040 x 2040 pixels in x/y and the z-step interval set to 1 μm
355 collecting a total of 40 μm in the z-axis direction. Fold-changes in normalized signal intensity were
356 quantified with background subtraction using Z-project Maximum Intensity Projection in FIJI and
357 further normalized to number of nuclei for GFAP and HIF-1α analyses.

358 ***2.13 MONHA-encapsulated hydrogel rheology analysis***

359 MONHA-encapsulated hydrogels, fabricated using the 10 x 6 mm PDMS molds, were
360 cultured for 14 days prior to application of biomechanical strain. Immediately following 24 hours
361 of mechanical loading, viscoelasticity of MONHA-encapsulated hydrogels (N = 6 per group) was
362 measured using a Kinexus rheometer (Malvern Panalytical, Westborough, MA, USA) with an 8
363 mm diameter parallel plate. Rheometry measurements were performed as previously described
364 [33, 49]. Briefly, an 8 mm geometry was lowered onto the hydrogels to establish a calibration

365 normal force of 0.02 N. Subsequently, an oscillatory shear-strain sweep (0.1–60%, 1.0 Hz, 25 °C)
366 was performed to determine storage modulus (G') and loss modulus (G") values within the linear
367 viscoelastic region. The storage modulus for each sample was then converted to elastic modulus
368 (E) using the equation E = 2 * (1 + v) * G', assuming a Poisson's ratio (v) of 0.5 for the ECM
369 hydrogels.

370 ***2.14 Statistical analyses***

371 Statistical analyses were performed using GraphPad Prism software v10.0.2 (GraphPad
372 Software, La Jolla, CA, USA). Experiments were conducted at least in triplicate. Individual sample
373 sizes are specified in each figure caption. Group comparisons were determined by one-way
374 (ANOVA) with Tukey's multiple comparisons *post hoc* as appropriate and Cohen's effect size d
375 as described in Methods 2.6 [44]. All data are shown with mean ± SD. The level of significance
376 was set to $p < 0.05$.

377

378 ***3. Results***

379 ***3.1 Characterization of MONHA-encapsulated hydrogel pore size, permeability, and regional***
380 ***differences.***

381 Under healthy conditions, local astrocytes create a honeycomb network spanning the
382 diameter of the rodent ONH [50]. Their processes can measure a thickness of 1.3 ± 0.04 μm with
383 elongations of up to 30 μm [51]. To determine whether our previously developed hydrogel system
384 was adequately porous to allow for astrocyte process elongation and coupling through the collagen
385 network, we first quantified the pore size of acellular hydrogels in the absence of biomechanical
386 strain. Using confocal reflectance microscopy to directly visualize collagen fibers within acellular

387 hydrogels, we observed that the collagen fibrils displayed a homogeneous network with pore sizes
388 ranging from 2-7 μm (Suppl. Fig. 1A-B).

389 Next, we quantified hydrogel permeability over time (Suppl. Fig. 1C). Since our MONHA
390 growth media contains primarily FBS proteins ranging < 60 – 70 kDa (with albumin being the
391 most abundant) [52, 53], and growth factor EGF of ~ 6 kDa [54], we chose to use a 70 kDa FITC-
392 labelled dextran tracer solution as an indicator for permeability. Both the acellular and MONHA-
393 encapsulated hydrogels showed robust permeability, as seen by the rapid detection of increased
394 fluorescence below the hydrogel within 5 minutes of adding FITC-labelled dextran solution to the
395 top of the hydrogels (Suppl. Fig. 1C). Thus, these results support that MONHA-encapsulated
396 hydrogels allow for efficient and adequate nutrient distribution.

397 To characterize the architecture of the ECM network within our MONHA-encapsulated
398 hydrogels, we evaluated the compaction of collagen fibrils. We observed regional differences
399 within our constructs such that samples at baseline (under no biomechanical strain) displayed
400 increased collagen compaction in the periphery of the hydrogel as compared to the core (Suppl.
401 Fig 2A-B). Moreover, the collagen compaction appeared greater immediately adjacent to astrocyte
402 cell bodies/processes (Suppl. Fig. 2A). Collectively, these data support that encapsulated ONH
403 astrocytes differentially remodel and contract their surrounding collagen fibers in the core as
404 compared to the unbound periphery of the hydrogel. Because of this heterogeneity in collagen
405 compaction, we artificially delineated the core from the periphery of MONHA-encapsulated
406 hydrogels for subsequent experiments and comparisons (Suppl. Fig. 2C).

407 ***3.2 Quantification of astrocyte cell viability within MONHA-encapsulated hydrogels after cyclic***
408 ***biomechanical strain.***

409 After characterizing the hydrogel system, we then applied compressive biomechanical
410 strains to MONHA-encapsulate hydrogels using a custom bioreactor [34-36]. We applied 3% and
411 10% compressive strains, which have been reported in ONH tissues during glaucomatous insult
412 [28-30]. After 24h of biomechanical strain, we quantified astrocyte cell viability in MONHA-
413 encapsulated hydrogels (Suppl. Fig. 3). We found no detectable difference in total viability by
414 MTS assay after biomechanical strain for 24h (Suppl. Fig. 3).

415 ***3.3 Biomechanical strain regulates global transcriptomic response of MONHAs across strain***
416 ***level and time***

417 Astrocytes within the ONH are transcriptionally responsive to alterations in IOP. Several
418 murine experimental glaucoma studies have investigated the effects of elevated IOP on ONH
419 astrocyte gene expression and downstream responses [19, 55, 56]. However, it is not clear how
420 glaucoma-associated *biomechanical strains* directly affect ONH astrocyte gene expression and
421 molecular pathways. Here, we investigated the transcriptional response of ONH astrocytes to
422 biomechanical strain across strain intensities and durations. Overall, all the RNA samples showed
423 high quality indicated by an RNA integrity number (RIN) ≥ 8.

424 To assess the global transcriptional effects of biomechanical strain on astrocytes, we
425 performed principal component analysis (PCA) on bulk RNA sequencing data from MONHA-
426 encapsulated hydrogels subjected to 0%, 3%, or 10% static compression for either 4 hours or 24
427 hours per hydrogel region (i.e., core or periphery). Within the core of the hydrogel, the first three
428 principal components (PC1, PC2, and PC3) accounted for a cumulative 84.5% of the total variance
429 in the dataset, with PC1(i.e., time) alone explaining 63.07% (Suppl. Fig. 4A). Within the periphery
430 of the hydrogel, the top three principal components accounted for 84.4% of total variance (PC1:
431 57.58%, PC2: 17.46%, PC3: 9.36%) (Suppl. Fig. 4B). PCA revealed that the duration of

432 biomechanical strain primarily drove transcriptional variation, with samples separating along PC1.
433 Strain dynamics in both regions were most observed with 10% strain revealing an initial significant
434 shift along PC2 and PC3 in the 4h groups and maintained in 24h groups. Overall, the PCA results
435 of both the core and periphery demonstrate that the responses of encapsulated MONHAs to
436 biomechanical stress are modulated in a time- and strain- dependent manner, with more
437 pronounced transcriptional changes observed under higher and prolonged strain compared to 0%
438 controls.

439 ***3.4 Pairwise analysis reveals distinct transcriptional responses dependent on magnitude of***
440 ***biomechanical strain and hydrogel region.***

441 Our initial investigation into the impact of biomechanical strain on MONHA-encapsulated
442 hydrogels focused on how different strain intensities (i.e., 3% or 10%) affect gene expression at
443 different timepoints (i.e., 4h or 24h). DESeq2 analysis identified 19,163 genes after 4h
444 biomechanical strain and 18,376 genes after 24h biomechanical strain. We applied a cutoff of FDR
445 ≤ 0.05 and fold change $|FC| \geq 1.5$. DEGs from the core of the hydrogel are depicted in Table 1 and
446 in Fig. 1 A, B and Fig. 2 A, B. To simplify the discussion, we have annotated groups by "magnitude
447 of strain" followed by "hydrogel region"; thus, the hydrogel core that underwent 3%
448 biomechanical strain is denoted as *3c*, while the hydrogel periphery is denoted as *3p*. In response
449 to both intensities of biomechanical strain, we observed fewer DEGs in the 24h group vs the 4h
450 group, supporting that encapsulated MONHAs adapt to biomechanical strain with increasing
451 durations (Table 1).

	4h	24h
3% vs 0%	**1,368 total DEGs** 686 upregulated, 682 downregulated	**377 total DEGs** 104 upregulated; 273 downregulated
10% vs 0%	**1,968 total DEGs** 880 upregulated; 1088 downregulated	**413 total DEGs** 147 upregulated; 266 downregulated

452 **Table 1.** DEGs with FDR ≤ 0.05 and fold change $|FC| \geq 1.5$, core of the hydrogel.

453 For all groups, to identify the functional categories the DEGs were enriched in, the list of
454 DEGs per comparison were uploaded to the publicly available WEB-based GEne SeT AnaLysis
455 platform. In the *3c* group after 4h biomechanical strain, over representation analysis (ORA)
456 revealed enrichment of GOs involved in cell-cell junction, collagen-containing ECM,
457 laminin/fibronectin binding, and cell proliferation and migration (Fig. 1C). With increased
458 magnitude of strain, the *10c* group after 4h biomechanical strain showed enriched pathways in the
459 regulation of immune/defense response, response to cytokine, mitochondrion, adenosine
460 triphosphate (ATP)/nucleotide binding, and regulation of programmed cell death (Fig. 1D). These
461 findings suggest that, with short duration of strain (4h), increased magnitude of biomechanical
462 strain induced a shift in DEGs enriched in morphology, ECM regulation, and cell proliferation
463 (3%) to enrichment in inflammation regulating and cell cycle/division-related pathways (10%)
464 (Fig. 1C, D).

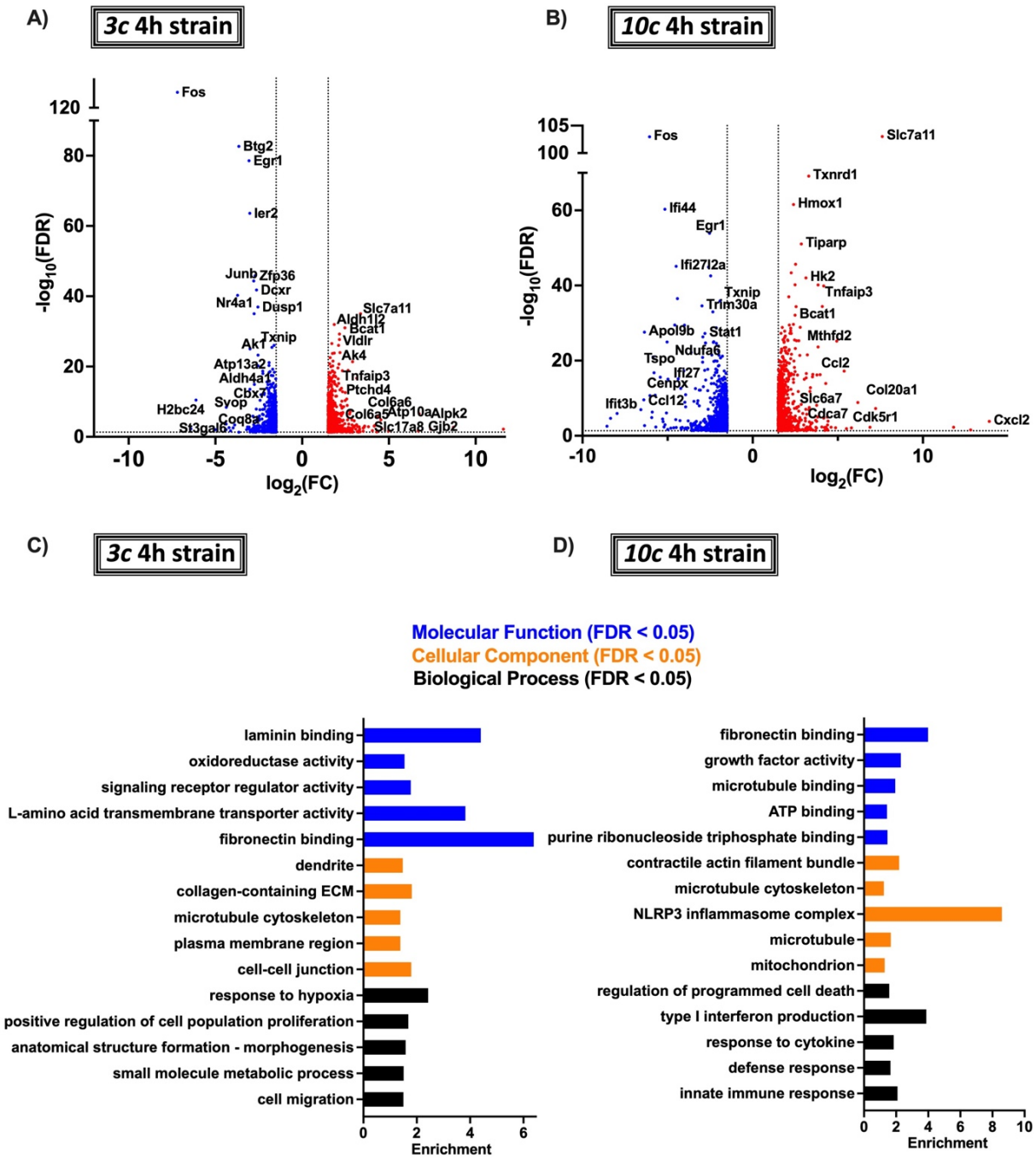

Fig. 1. Pairwise transcriptional mechanoresponse of MONHAs encapsulated within the hydrogel core to 4h of biomechanical strain. (A-B) Volcano plots representing the number of DEGs with FDR ≤ 0.05 and |FC| ≥ 1.5 in response to 3% and 10% biomechanical strain for 4h. **(C-D)** Listed are five representative gene ontology (GO) pathways per functional group of the top 30 most significant GOs at each timepoint.

474 Similar analyses were done for MONHAs undergoing biomechanical strain for 24h. For
475 the *3c* group after 24h biomechanical strain, GOs showed genes enriched in cell cycle, DNA
476 replication, organelle fission, condensed chromosome, microtubule associated complex, DNA
477 helicase activity and ATP binding (Fig. 2C). In contrast, in the *10c* group after 24h biomechanical
478 strain, GOs showed enriched genes in pathways of carbohydrate/AMP binding, response to
479 hormone, cell-substrate junction, response to hypoxia, and oxidoreductase activity (Fig. 2D).
480 These findings suggest that application of biomechanical strain for longer durations (24h) induces
481 a shift in DEGs enriched cell cycle and division pathways (3%) to enrichment in metabolism and
482 ECM regulatory pathways (10%) (Fig. 2C, D).
483

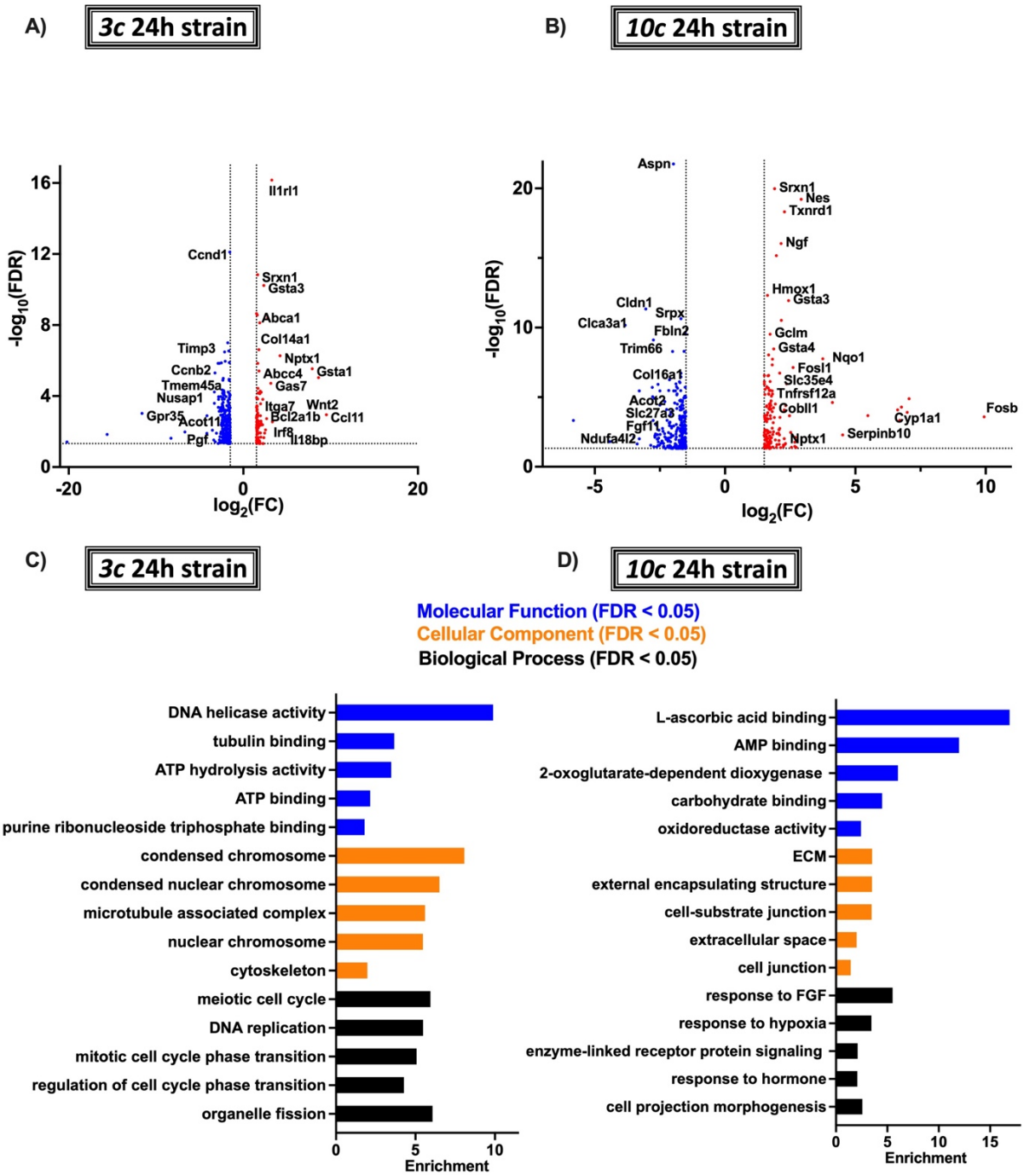

Fig. 2. Pairwise transcriptional mechanoresponse of MONHAs encapsulated within the hydrogel core to 24h of biomechanical strain. (A-B) Volcano plots representing the number of DEGs with FDR ≤ 0.05 and |FC| ≥ 1.5 in response to 3% and 10% biomechanical strain for 24h. **(C-D)** Listed are five representative gene ontology (GO) pathways per functional group of the top 30 most significant GOs at each timepoint.

491 We then analyzed the periphery of the hydrogel, where cells were surrounded by more
492 densely packed ECM (Suppl. Fig. 2). Again, we applied a cutoff of FDR ≤ 0.05 and fold change
493 |FC| ≥ 1.5; DEGs from the periphery of the hydrogel are depicted in Table 2 and in Suppl. Fig. 5
494 A, B and Suppl. Fig. 6 A, B.

	4h	24h
3% vs 0%	**688 total DEGs** 336 upregulated, 352 downregulated	**13 total DEGs** 6 upregulated; 7 downregulated
10% vs 0%	**801 total DEGs** 322 upregulated; 479 downregulated	**445 total DEGs** 112 upregulated; 333 downregulated

495 **Table 2.** DEGs with FDR ≤ 0.05 and fold change |FC| ≥ 1.5, periphery of the hydrogel.

496 In this peripheral region, for relatively short duration biomechanical strain (4h), we
497 similarly observed that MONHAs displayed a shift in DEGs enriched in cellular signaling
498 regulation (*3p*) to inflammation and metabolism pathways (*10p*) (Suppl. Fig. 5C, D). Interestingly,
499 analysis of the *3p* group after 24h biomechanical strain identified few DEGs with no significant
500 GOs by our FDR cutoff values. The *10p* group after 24h biomechanical strain showed GOs
501 primarily enriched in ECM regulation and adhesion (Suppl. Fig. 6C).

502 Taken together, these transcriptomic and functional analyses provide new insights into
503 astrocyte responses to isolated biomechanical stimulation.

504 ***3.5 Hydrogel region and duration of biomechanical strain modulate key astrocytic molecular***
505 ***and metabolic pathways***

506 To investigate the contribution of increasing magnitude and duration of biomechanical
507 strain to MONHA transcriptional response, we performed ANOVA of biomechanical strain groups
508 across timepoints followed by GSEA against both KEGG and Reactome databases. In the hydrogel
509 core, encapsulated astrocytes downregulated pathways related to focal adhesions *(Col6a6; Flnc;*
510 *Flt1; Hgf; Itga10)*, integrin cell surface interactions *(Itga5; Itga7; Itgb3; Itgb8; Lama2)*, and ECM
511 interactions *(Col6a5; Col6a6; Itga10; Tnxb)* (Fig. 3A, B, D). These altered pathways corroborate

512 our findings on genes enriched in GOs associated with cell morphology and ECM reorganization.
513 Biomechanical strain on encapsulated astrocytes also led to the downregulation of key signaling
514 pathways regulating astrocyte quiescence, including those regulating stem cell pluripotency *(Rest;*
515 *Tbx3; Wnt11)*, calcium signaling *(Camk2a; Fzd3; Fzd4),* interleukin-6 (IL6) *(Clcf1; Cntfr; Il6ra;*
516 *Lif; Lifr; Osmr)*, phosphoinositide 3-kinase Ak strain transforming (PI3K-Akt) (*Bcl2l11; Chuk;*
517 *Vegfa; Flt3l; Gdnf; Hgf; Il6ra)*, and Wnt signaling *(Wnt11; Wnt5a)* (Fig. 3A, B, D).

518 Additionally, MONHAs encapsulated within the core of the hydrogel showed significant
519 changes in metabolism with increasing time and magnitude of strain. Specifically, we observed
520 upregulated pathways related to metabolic and respiratory electron transport chain (ETC) (Fig. 3A,
521 B, C). As a part of the mitochondrial oxidative phosphorylation, the ETC is crucial for ATP
522 production. These upregulations corresponded with gene enrichment in metabolism/ETC
523 complexes and in thermogenesis (*Acot2, Aldh1a1, Acy1, Adh7, Atp6v0d2, Cox6b1, Cox7a2,*
524 *Cox7b, Cox7c, Cox8a, Ndufa1, Ndufa11, Ndufa12,* and *Ndufb8)* (Fig. 6A-C*)*. Interestingly,
525 pathways for both cell cycle/repair *(Ccnb1; Ccnb2; Ccne1; Cdc20; Cdc45; Cdk1; Cdk18; Chek2)*
526 and cellular senescence *(Ccna2; Ccne2; Foxm1; Map2k6; Rbl1; Rras)* were also upregulated (Fig
527 3A-C), potentially indicating a cytoprotective stress response to increasing biomechanical strain
528 over time.

529 We then investigated the <u>hydrogel periphery</u>, where astrocytes were surrounded by a denser
530 ECM at baseline. Here, we found that peripheral MONHAs also downregulated pathways related
531 to cell cycle, mitosis, DNA synthesis, replication, and repair, ATP activation in response to
532 replication stress, and chromosome maintenance, but observed a lack of IL6/Wnt signaling
533 pathways (Suppl. Fig. 7A-D).

534 Collectively, these findings reveal that biomechanical strain plays a crucial role in
535 modulating astrocyte mechano-transcriptional response. Specifically, increased strain over time
536 induces downregulation of pathways related to cell structure and signaling while upregulating
537 metabolic and stress response pathways, possibly indicating an attempt at maintaining cellular
538 function and survival. Conversely, a denser ECM in the hydrogel periphery may provide a level
539 of protection to increasing compressive strain over time and, as such, it may dampen the pro-
540 inflammatory reactive astrocyte phenotype and modulate cell cycle, suggesting a link between
541 ECM composition and astrocyte-mediated inflammation. These astrocyte transcriptional profiles
542 elucidate the complex changes over time interlinking biomechanical forces, ECM density, and
543 cellular mechanoresponse.

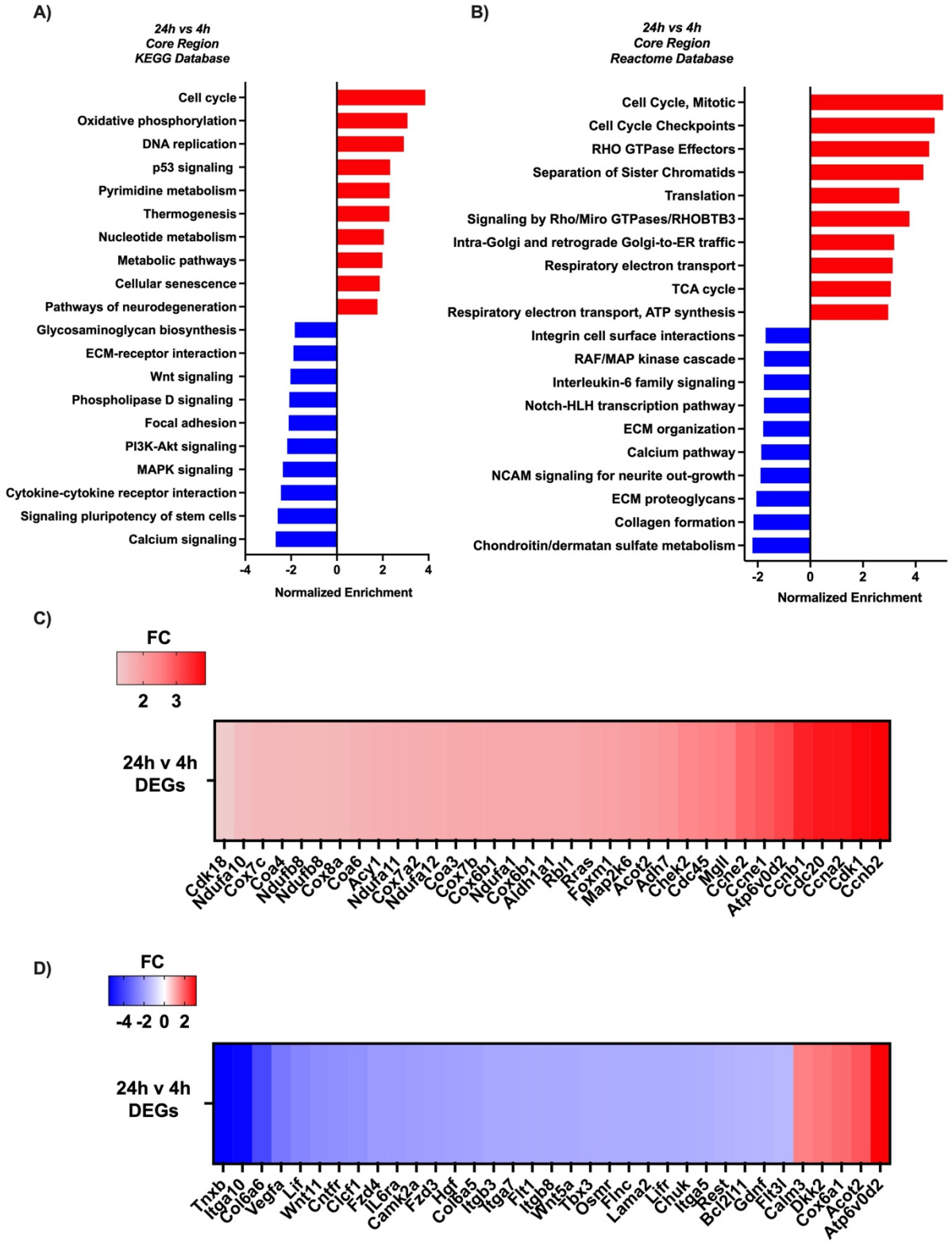

Fig. 3. Transcriptional mechanoresponse of MONHAs encapsulated within the hydrogel core over time with increasing strain. (A-B) Listed here are 20 up and down most significant pathways against KEGG and Reactome databases with representative 35 DEGs for the **(C)**

548 upregulated and **(D)** downregulated pathways (FDR ≤ 0.05 and |FC| ≥ 1.5) based on ANOVA
549 analysis of MONHAs mechanoresponse over time (i.e., 24h vs 4h) with increasing strain.

550 ***3.6 Increased compressive strain alters MONHA cytoskeletal architecture.***

551 Immediately following glaucomatous insult, ONH astrocytes respond by reorienting their
552 cell bodies and remodeling their F-actin cytoskeleton architecture [18, 20-23, 51]. Given that
553 transcriptomic analyses showed an enrichment in genes regulating cell process and cytoskeletal
554 organization, we asked whether isolated biomechanical strains would alter MONHA morphology
555 and cytoskeletal architecture in absence of other key *in vivo* microenvironmental cues. To do so,
556 we quantified F-actin area coverage and levels of GFAP expression in MONHA-encapsulated
557 hydrogels after biomechanical strain application for 4h and 24h, respectively.

558 After 4h cyclic biomechanical strain, MONHAs showed no significant changes in F-actin
559 area coverage in either the core or periphery of the hydrogels (Fig. 4A-C). In contrast, after 24h of
560 cyclic biomechanical strain, there was a significant drop in F-actin area coverage within the core
561 of the hydrogel in a strain-dependent manner (Fig. 4A-C). Both *3c* and *10c* groups showed ~50%
562 decrease in F-actin area coverage compared to control (0%) (Fig. 4C). Interestingly, application of
563 biomechanical strain did not alter the F-actin area coverage in the periphery of the hydrogel in
564 either strain group (Fig. 4C). Consistent with the observed F-actin remodeling, encapsulated
565 MONHAs showed varied cell alignment in response to duration and magnitude of strain (Suppl.
566 Fig. 8). While both 4h groups and periphery groups had no effect on cell alignment, the *10c* group
567 demonstrated a significant increase in astrocyte alignment in response to biomechanical strain
568 (Suppl. Fig. 8B). Overall, these data demonstrate that encapsulated MONHAs are robustly
569 mechanoresponsive, altering cellular morphology in response to biomechanical stimuli.

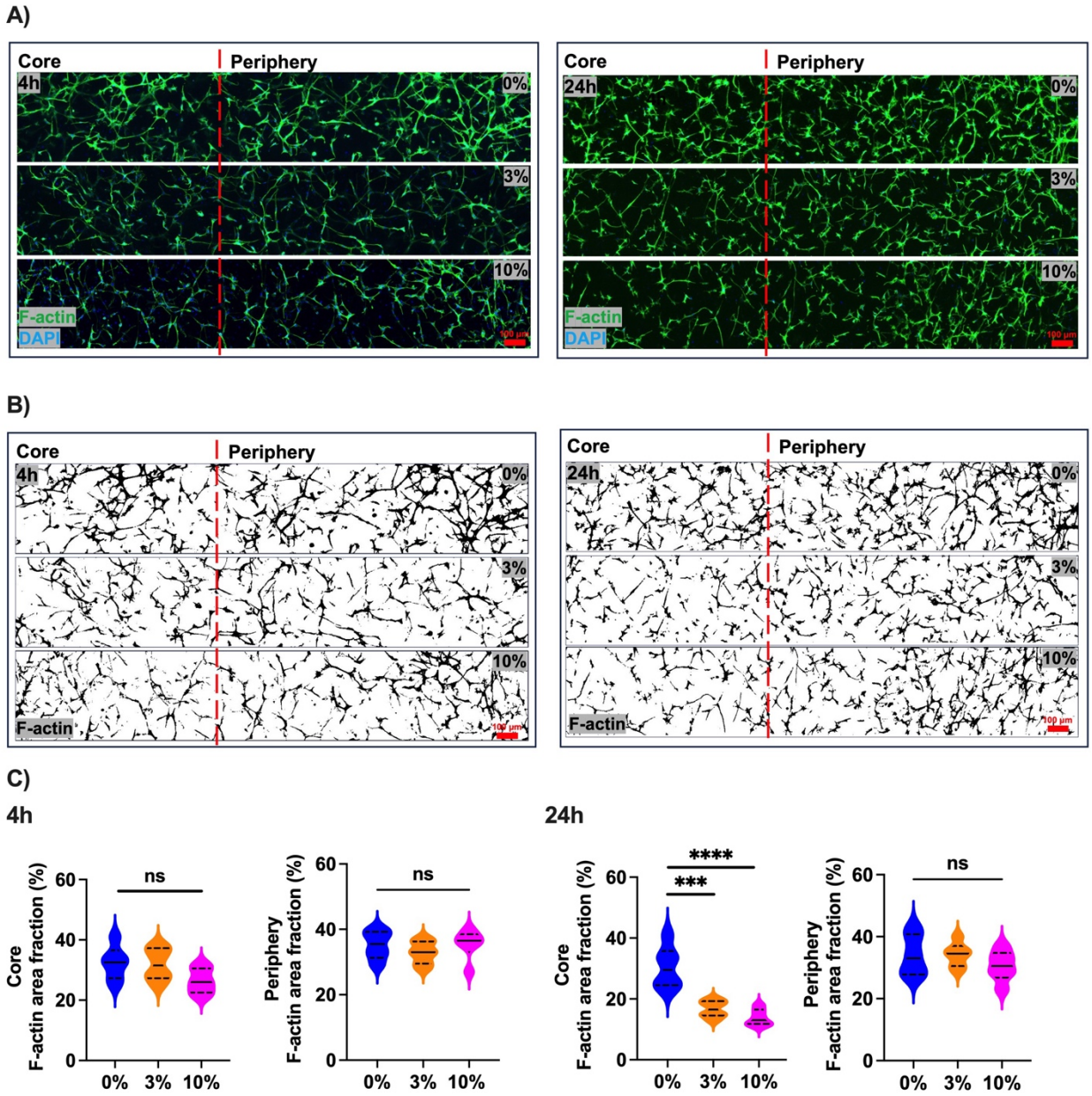

Fig. 4. Regional differences in MONHA morphology in response to duration and magnitude of biomechanical strain. (A) Representative fluorescence images of astrocyte F-actin staining (A) and cytoskeletal binarized masks (B). Scale bar: 100 µm. **(C)** Quantitative analyses of F-actin mask area (N = 6 fields of view/group). Statistical significance was determined using one-way ANOVA (*$p < 0.05$, **$p < 0.01$, ***$p < 0.001$, **** $p < 0.0001$) for F-actin area fraction analyses.

Astrocytes respond to glaucomatous insults within the ONH by undergoing reactive gliosis, in part characterized by an increase in expression of intermediate filaments such as GFAP [4, 57, 58]. We previously showed that both MONHAs in 2D and encapsulated within 3D hydrogels can

be induced to express higher levels of GFAP upon stimulation with a known inducer of astrocyte reactivity such as exogeneous TGFβ2 [33, 37]. Therefore, we asked whether application of cyclic biomechanical strain would induce a similar induction in intermediate filaments. Control (0% compression) MONHA-encapsulated hydrogels showed baseline immunoreactivity of GFAP throughout the hydrogel. After both 4h and 24h of biomechanical strain, GFAP immunolabeling increased ~1.5 fold in both the core and periphery of the hydrogel (Fig. 5A-C, Suppl. Fig. 9A-C). As such, these data support that biomechanical strains directly induce cytoskeletal alterations in encapsulated astrocytes.

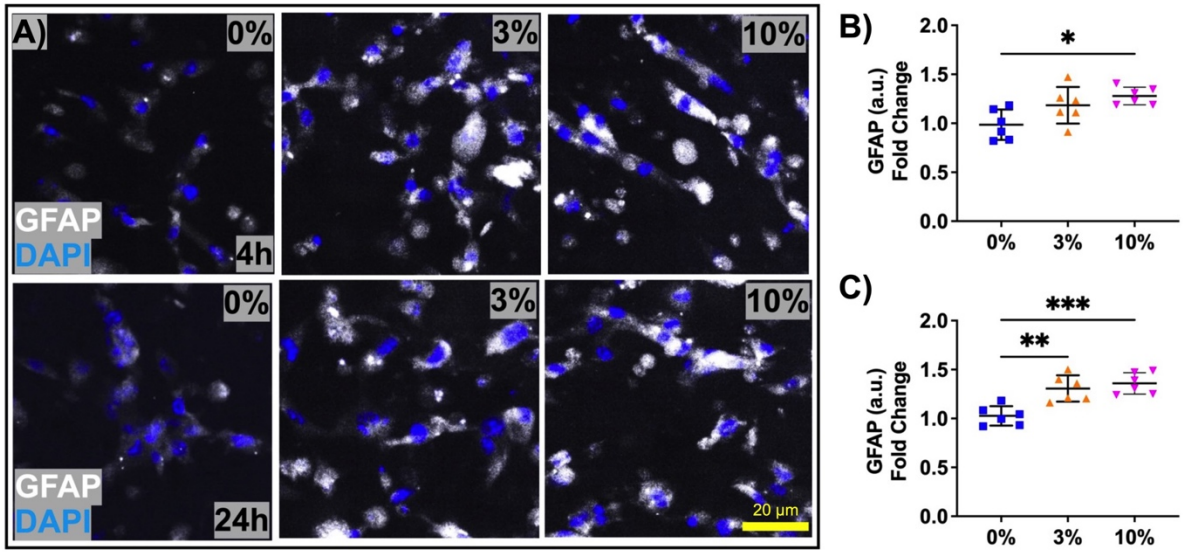

Fig. 5. GFAP expression of encapsulated-MONHAs within the hydrogel core in response to biomechanical strain. (A) Representative fluorescence images and quantification of fold change in astrocyte GFAP signal intensity (N = 6 fields of view/group) after 4h **(B)** and 24h **(C)** of increasing strain (i.e., 3% or 10%). Statistical significance was determined using one-way ANOVA (*$p < 0.05$, **$p < 0.01$, ***$p < 0.001$) for GFAP expression levels. Scale bar: 20 µm.

3.7 Biomechanical strain alters HIF-1α levels within MONHA-encapsulated hydrogels.

Glaucomatous insults are associated with hypoxia and metabolic stress within the retina and ONH since IOP-induced deformations can impact the local vasculature and reduce

599 oxygenation of the ONH [59-61]. Since our transcriptomic data revealed many altered pathways
600 pertaining to cellular response to stress and hypoxia, and altered metabolic processes, we asked if
601 astrocytes within our model could modulate expression of HIF, thereby potentially affecting
602 downstream metabolic activity. Specifically, to determine whether encapsulated MONHAs
603 undergo such metabolic stress in response to cyclic biomechanical strain, we examined levels of
604 HIF-1α after application of biomechanical strain. HIF-1α immunoreactivity was low in control
605 (0%) samples at both timepoints (i.e., 4h and 24h; Fig. 6, Suppl. Fig. 10) regardless of hydrogel
606 region (i.e., core vs periphery). Hydrogel-encapsulated MONHAs exhibited significantly
607 increased HIF-1α levels by ~1.25-fold in the core groups after 4h cyclic biomechanical strain and
608 by ~2-fold in the periphery (Fig. 6A, B); HIF-1α also increased ~1.5-2-fold after 24h cyclic
609 biomechanical strain (Fig. 6A, C). Similar trends of HIF-1α elevation were observed in the
610 periphery of the hydrogel (Suppl. Fig. 10). Taken together, these data support that cyclic
611 biomechanical strain can directly induce metabolic insufficiency.

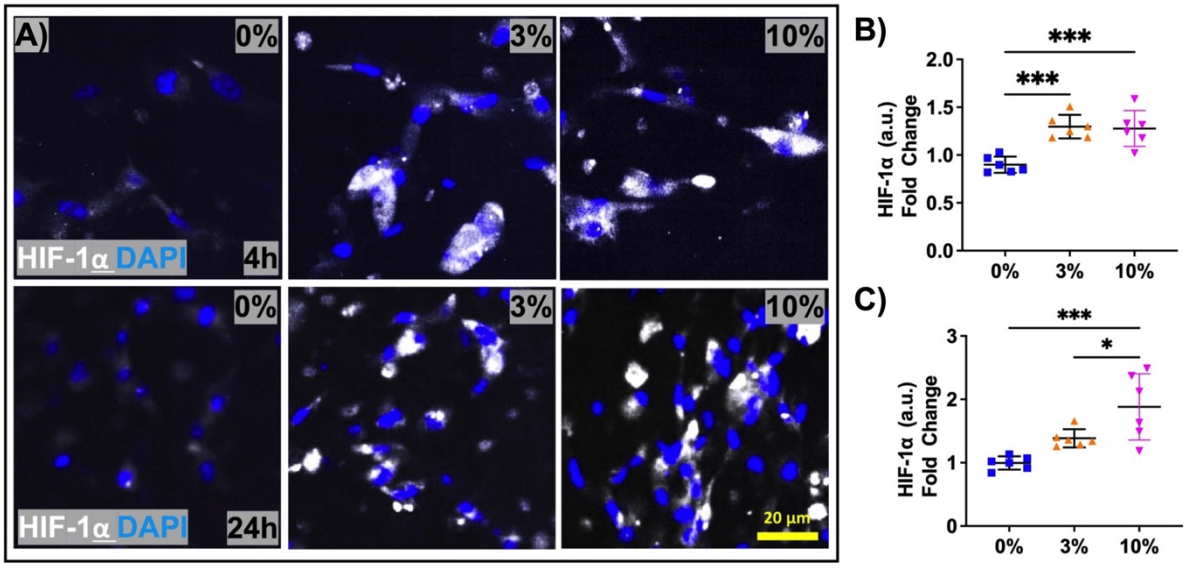

612

613 **Fig. 6. HIF-1α expression of encapsulated-MONHAs within the hydrogel core in response to**
614 **biomechanical strain. (A)** Representative fluorescence images and quantification of fold change
615 in astrocyte HIF-1α expression signal intensity (N = 6 fields of view/group) after 4h **(B)** and 24h

616 of increasing strain (i.e., 3% or 10%). **(C)**. Statistical significance was determined using one-way
617 ANOVA (*$p < 0.05$, **$p < 0.01$, ***$p < 0.001$) for HIF-1α expression levels. Scale bar: 20 μm.
618
619 ***3.8 Biomechanical strain on MONHA-encapsulated hydrogels induces matrix remodeling via***
620 ***collagen network remodeling and fibronectin deposition.***

621 Our transcriptomic analyses showed a strong enrichment in genes related to collagen and
622 ECM modulation. *In situ,* ONH astrocytes can modulate their surrounding ECM via secretion of
623 crosslinking and/or degrading enzymes [24, 57]. Therefore, we asked how application of cyclic
624 biomechanical strain would influence astrocyte modulation of the ECM microenvironment. We
625 first performed confocal reflectance microscopy to directly visualize collagen fibers within
626 MONHA-encapsulated hydrogels after biomechanical strain. We previously showed that control
627 constructs (0%) display regional differences in collagen arrangement, with more uniformly
628 distributed collagen fibers within the core of the hydrogel, and an increased density of collagen
629 fibers in the periphery of the hydrogel (Suppl. Fig. 2). While 4h of cyclic biomechanical strain did
630 not induce significant remodeling of the collagen fibrils across groups, after 24h biomechanical
631 strain, both 3% and 10% showed significant *decrease* of collagen compaction within the core (Fig.
632 7A, B) and a significant *increase* in collagen compaction in the periphery compared to control
633 (0%) (Suppl. Fig. 11A, B). Collectively, these data support that application of cyclic
634 biomechanical strain for 24h significantly alters collagen compaction in a region-dependent
635 manner.

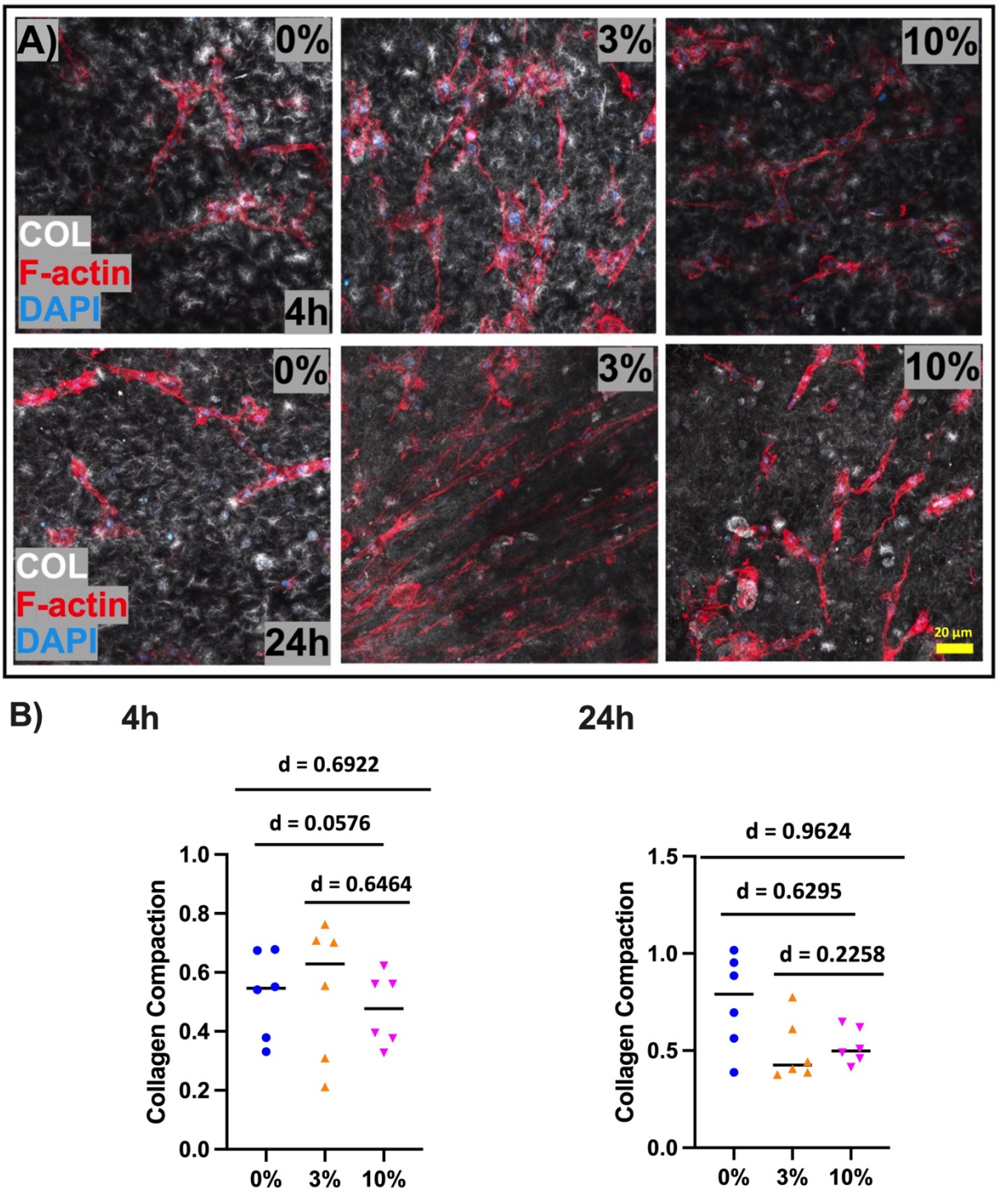

Fig. 7. ECM collagen fibrils remodeling in the core of MONHA-encapsulated hydrogels in response to biomechanical strain. (A) Representative fluorescence images of collagen fibrils remodeling in response to duration (i.e., 4h or 24h) and magnitude of strain (i.e., 3% or 10%) (N = 6 fields of view/group). Scale bar: 20 µm. **(B)** Quantification of collagen compaction post strain.

Cohen's effect size d (Cohen's d = 0.20, 0.50, and 0.80 is used to indicate the effect sizes as small, medium, or large, respectively).

Reactive astrocytes increase secretion of key ECM scaffold proteins such as fibronectin. This glycoprotein can also interact with other ECM proteins (i.e., collagen I and laminin) further promoting matrix crosslinking and, thus, contribute to the stiffening and fibrosis of the ONH tissue [24, 57, 62-65]. As such, we investigated how biomechanical strain impacts astrocyte secretion of fibronectin. Across all groups, biomechanical strain increased fibronectin deposition in MONHA-encapsulated hydrogels (Fig. 8). After 4h of biomechanical strain, hydrogels showed a ~2.5-3-fold increase in fibronectin immunolabeling within the core, and a ~1.5-fold increase within the periphery (Fig. 8 A, B). Similar trends were observed with 24h of biomechanical strain, such that the core displayed a ~6-fold increase (Fig. 8 A, C), and the periphery of the hydrogels had a less robust ~2-fold increase in fibronectin immunolabelling (Suppl. Fig. 12).

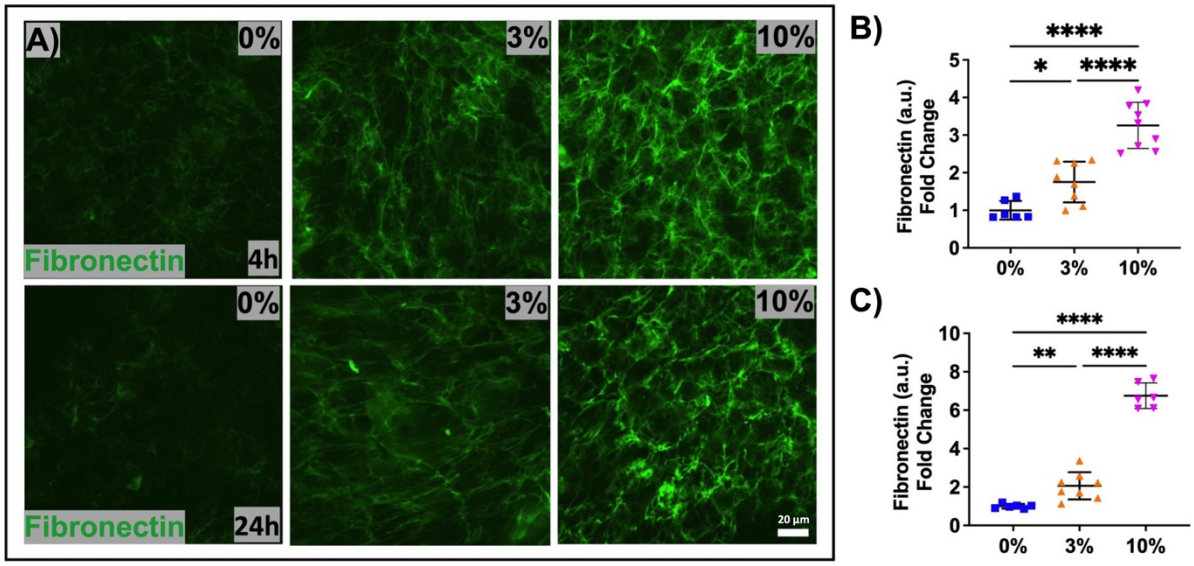

Fig. 8. ECM fibronectin secretion in the core of MONHA-encapsulated hydrogels in response to biomechanical strain. (A) Representative fluorescence images of fibronectin in response to duration (i.e., 4h or 24h) and magnitude of strain (i.e., 3% or 10%) (N = 6 fields of view/group) and **(B-C)** quantification of fold change in fibronectin signal intensity. Statistical significance was determined using one-way ANOVA (*$p < 0.05$, **$p < 0.01$, **** $p < 0.0001$) for fibronectin signal intensity. Scale bar: 20 µm.

662 The observed alterations in ECM protein compaction and deposition could potentially
663 impact the global stiffness of MONHA-encapsulated hydrogels. Thus, we analyzed the overall
664 rheological properties of hydrogels after biomechanical strain. After application of 3% or 10%
665 biomechanical strain for 24h, we found no significant differences in hydrogel stiffness compared
666 to their uncompressed (0%) controls (Suppl. Fig. 13).

667 Collectively, these data show that cyclic biomechanical strain significantly alters collagen
668 distribution and astrocyte fibronectin production in MONHA-encapsulated hydrogels, indicating
669 a dynamic interplay between mechanical stimuli, ECM remodeling, and astrocyte
670 mechanoresponse.

671

672 ***4. Discussion***

673

674 Mechanical injury is a driving factor in the pathogenesis of several CNS disorders,
675 including traumatic brain injury, spinal cord injury, and glioma [7, 66-68]. In glaucoma, increased
676 biomechanical strains on the ONH have long been associated with elevated IOP and disease
677 progression [28-30, 57]; and yet, the mechanoresponse of ONH resident cells remains poorly
678 understood. ONH astrocytes have emerged as key regulators of retinal ganglion cell axonal health.
679 In *in vivo* glaucoma models, these local astrocytes are amongst the first to respond by reorganizing
680 their cytoskeleton architecture and gap junction coupling [18, 20-23, 51]. In the present study, we
681 sought to comprehensively analyze the direct transcriptional and functional responses of astrocytes
682 to glaucomatous biomechanical strains, to better understand the role of these pathologic
683 biomechanical forces on astrocyte behavior.

684 ***Dissecting the ONH astrocyte mechanoresponse by modeling glaucomatous biomechanical***
685 ***strains in a 3D ECM hydrogel system***

686 Prior studies have explored ONH astrocyte mechanoresponse to glaucomatous
687 biomechanical strains using conventional 2D *in vitro* cultures [27, 69]. However, it is increasingly
688 recognized that the ECM significantly influences cell behavior, with mechanical, structural, and
689 compositional cues playing critical roles in modulating cell function [70]. Newer *in vitro* 3D
690 models, including our own, utilize viscoelastic ECM biopolymer hydrogels such as collagen and
691 hyaluronic acid to better mimic the 3D architecture and promote a more natural astrocyte
692 morphology [33, 71, 72]. By encapsulating astrocytes within a collagen/hyaluronic acid network,
693 one can directly visualize cell-cell and cell-ECM interactions. We previously showed that
694 encapsulated murine ONH astrocytes extend processes in 3D, couple with astrocyte neighbors,
695 and bind to and modify their surrounding ECM [33]. In this study we sought to comprehensively
696 investigate how 3D-encapsulated ONH astrocytes respond to glaucoma-related biomechanical
697 strains over time. A custom bioreactor has been used on rat cortical astrocytes encapsulated in
698 collagen to dissect their mechanoresponse to compression [34]. Building on this prior work, we
699 used a newer version of the same 3D compressive bioreactor to apply increasing intensities of
700 biomechanical strain over time (i.e., in 4D) to investigate nuanced ONH astrocyte mechano-
701 transcriptomic and morphometric responses to mechanical stimuli.

702 ***Biomechanical strain triggers a multifaceted transcriptomic and functional response in ONH***
703 ***astrocytes***

704 Five main functional responses were observed in this study. Hydrogel-encapsulated murine
705 ONH astrocytes demonstrated transcriptomic alterations in (i) proliferation/senescence, (ii)
706 cytoskeletal architecture, (iii) metabolic function, (iv) inflammation, and (v) ECM remodeling in

707 response to mechanical strain. Many astrocytic genes revealed enrichment in DNA replication,
708 mitotic cell cycle and chromosomal dynamics, as well as cellular senescence and p53 signaling.
709 Early in *in vivo* glaucoma models, ONH astrocytes proliferate, and exhibit increased reactive
710 gliosis [19, 23, 73]. With prolonged IOP elevation, ONH astrocytes show evidence of cell
711 senescence and death [74, 75]. Interestingly, in our study, transcriptional alterations did not
712 correlate with a change in astrocyte viability in response to relatively short durations of
713 biomechanical strain of 4h and 24h. Future studies will examine astrocyte senescence/death in
714 response to longer durations of biomechanical strain.

715 ***Biomechanical strain induces alterations of astrocyte cytoskeletal architecture and intracellular***
716 ***signaling pathways***

717 There is *in vivo* evidence that ONH astrocytes undergo a dramatic reorientation of their F-
718 actin cytoarchitecture within 8 – 72 h of acute IOP elevation [18, 21-23]. In our study, hydrogel-
719 encapsulated murine ONH astrocytes downregulated pathways of focal adhesion and ECM-
720 interactions, and genes were enriched in GOs pertaining to morphological changes such as
721 cytoskeleton, actin-based cell projection, dendrite and cell-cell junction. *In vivo* glaucoma models
722 also depict a decrease in astrocyte process complexity and coupling [51, 74], potentially reducing
723 astrocyte-astrocyte connectivity as well as contact with surrounding blood vessels, retinal ganglion
724 cell axons, and ECM. Similarly, in response to both 3% and 10% biomechanical strain, we showed
725 a trend in decreased murine ONH astrocyte F-actin coverage after 4h of biomechanical strain that
726 significantly worsened with increasing magnitude and duration of strain. Thus, the observed
727 downregulation of focal adhesion and ECM-interaction regulatory pathways, coupled with
728 decreased F-actin coverage under biomechanical strain suggests a significant compromise in the
729 structural and functional integrity of the 3D astrocytic network. As such, a lack of adequate

730 astrocyte-astrocyte communication and interactions with surrounding ECM may further propagate
731 glaucomatous damage.

732 A key feature of the glaucomatous ONH is the onset of reactive astrogliosis and the
733 development of a pro-inflammatory astrocyte phenotype [14, 23, 57, 58, 76]. This is particularly
734 evidenced by the upregulation of intermediate filaments like GFAP, vimentin, and nestin, along
735 with the secretion of inflammatory cytokines [4, 12]. Consistent with these observations, our study
736 found enrichment of genes related to astrocyte reactivity and inflammation. Moreover, cytoskeletal
737 alterations can disrupt intracellular calcium signaling [57, 77, 78] . In our model, increased
738 biomechanical strain downregulated pathways like stem cell pluripotency, calcium signaling, IL6,
739 PI3K-Akt, and Wnt signaling. Consistent with the variability of F-actin cytoskeletal changes we
740 observed within our system (i.e., decreased F-actin coverage in the core, but not periphery),
741 hydrogel-encapsulated murine ONH astrocytes also displayed a range of GFAP upregulation.
742 Notably, the highest GFAP expression was observed in astrocytes located within the core of the
743 ECM hydrogel after 24h of biomechanical strain. In line with our RNAseq data, this heightened
744 reactivity may stem from altered calcium signaling as a direct result of strain-induced F-actin
745 cytoskeletal remodeling [78]. As such, these cellular changes depict the intricate relationship
746 between biomechanical forces and astrocyte cytoskeletal/signaling dynamics, and its crucial role
747 in ONH astrocyte pathogenesis.

748 In glaucoma models, the optic nerve undergoes hypoxia and metabolic insufficiency,
749 correlating with increased glycolysis and ATP production [15, 60, 61, 79]. In response to
750 biomechanical strain, we observed altered pathways related to hypoxia and oxygen levels. Within
751 4h of biomechanical strain, genes were enriched in cell response to hypoxia pathways and
752 maintained at longer durations (24h). These transcriptional changes correlated with increased HIF-

753 1α expression, which can trigger transcription of hypoxia-responsive genes, affecting downstream
754 metabolism [61, 80, 81]. We also observed upregulated metabolic and respiratory electron
755 transport/ATP synthesis pathways with genes enriched in mitochondrion and ATP binding. Thus,
756 our data highlight the important role of biomechanical strain in modulating astrocyte metabolic
757 function. Moreover, metabolic dysfunction, including altered glycolysis and ATP production, is
758 intertwined with pathways regulating cell survival and death, and can trigger cellular senescence
759 [60, 82]. These processes are increasingly recognized as key contributors to the pathogenesis of
760 glaucoma [83]. Further understanding the metabolic-cell senescence interplay in response to
761 longer durations of biomechanical strain and alterations of oxygen availability is crucial for
762 elucidating the mechanisms driving ONH astrocyte dysfunction in glaucoma.

763 ***ECM Integrity Modulates Astrocyte Response to Biomechanical Strain***

764 In disease, astrocytes modify the ECM extensively, leading to increased ECM protein
765 production and crosslinking [24, 57, 62, 63]. Here, our transcriptomic analyses revealed a
766 significant enrichment of genes associated with collagen, fibronectin, and ECM modulation. More
767 specifically, we denoted downregulated pathways related to ECM-receptor interaction, integrin
768 cell surface interactions, ECM proteoglycans and ECM organization. Accordingly, we observed
769 differences in collagen fiber density after biomechanical strain. After 24h of strain, there was a
770 significant reduction in collagen compaction surrounding the ONH astrocytes in the core of the
771 hydrogel, suggesting that the observed changes in F-actin area coverage may diminish cell-ECM
772 interactions, resulting in a decreased ability to remodel surrounding collagen fibrils. Similar to the
773 glaucomatous ONH [24, 57, 62-65], we also found increased fibronectin levels in hydrogel-
774 encapsulated murine ONH astrocytes after biomechanical strain. Astrocyte-driven ECM
775 remodeling, prompted by increased biomechanical strain, may exacerbate glaucomatous injury

776 [84]. Future studies targeting astrocyte-mediated ECM modulation are warranted to explore the
777 restoration of ECM homeostasis to prevent further glaucomatous damage.

778 Interestingly, we found certain divergent ECM phenotypes in the periphery of the hydrogel,
779 with collagen fibers showing greater compaction with increasing magnitude and duration of
780 biomechanical strain. While biomechanical strain resulted in gene enrichment in cell cycle and
781 ECM regulation, and increased expression levels of GFAP, HIF-1α, and fibronectin (similar to the
782 core astrocytes), there was greater gene enrichment in mitochondrion, small metabolic process,
783 and ROS. Notably, there were pathways upregulated in cell cycle/stress, oxidative phosphorylation
784 and organelle protein trafficking (motor proteins, DNA replication, activation of ataxia
785 telangiectasia and Rad3 related (ATR) in response to replication stress, Golgi to ER transport),
786 and downregulated reactivity/inflammation (interleukin 17 (IL17), mammalian target of
787 rapamycin (mTOR), PI3K-Akt, cytokine-cytokine interaction, calcium signaling). Also in this
788 region, F-actin area coverage and process complexity remained unchanged after biomechanical
789 strain and showed *increased* collagen compaction (in contrast to the core of the hydrogel). The
790 difference in transcriptomic and phenotypic response is quite curious and highlights the important
791 role that surrounding ECM integrity plays in astrocyte response to biomechanical strain.

792 ***Limitations and Future Directions***

793 While the current *in vitro* hydrogel model offers a more controllable microenvironment to
794 study the complex mechanoresponses of ONH astrocytes, it also presents inherent limitations when
795 used to mimic the intricate *in vivo* biomechanical loading of the optic nerve head in glaucoma [24,
796 28-30, 57]. Here, we encapsulated murine ONH astrocytes in a fibrillar ECM hydrogel, which does
797 not precisely recapitulate the complex composition of a primate lamina cribrosa nor a murine
798 astrocytic lamina [62, 85, 86]. In the future, the hydrogel system could be modified by ECM

799 patterning, to generate a more representative lamina cribrosa-like structure. Many of our insights
800 into mechanisms of glaucoma pathophysiology are gained from experimental rodent models [14,
801 15, 20, 21, 50, 51, 55, 87-89]. To compare/contrast the effects of isolated biomechanical strain on
802 ONH astrocyte behavior to existing *in vivo* model systems, here, we encapsulated *murine* ONH
803 astrocytes. Our model system does allow for the incorporation of other resident cells, including
804 microglia or human ONH cell types, enabling analysis of cell-cell interactions under
805 biomechanical strain. It is important to note that our study used static 0% strain as controls, while
806 astrocytes *in vivo* experience constant biomechanical loading as baseline [24, 28-30, 57]. The
807 benefit of encapsulating cells within 3D ECM biopolymers is the ability of the cells to directly
808 interact with and modify these polymers [11, 90-92] (as seen in Suppl. Fig. 2). This supports that
809 encapsulated astrocytes experience a baseline level of biomechanical strain [93]. Consequently,
810 our study reports on the effects of *superimposed* compressive biomechanical strain on
811 encapsulated MONHAs. Future studies can modify superimposed strain and frequency
812 appropriate for the species of origin (i.e., murine cells vs. human cells). Lastly, our astrocyte-
813 encapsulated hydrogel model system is compatible with other bioreactors, such as the FlexCell
814 tension system [94, 95], permitting future live-cell imaging to investigate the mechanisms
815 governing mechanotransduction of ONH cells in glaucoma.

816 ***Conclusions***

817 Taken together, our transcriptomic and morphometric data provide new insights into ONH
818 astrocyte responses to isolated biomechanical stimulation. As the key mechanosensors of the
819 ONH, astrocytes are critical for initiating complex molecular cascades that can result in both
820 protective and detrimental outcomes, underscoring the importance of studying their nuanced
821 mechanoresponse. These responses are highly dependent upon dynamic astrocyte-ECM

822 interactions. Thus, our astrocyte-encapsulated ECM hydrogel is ideal for investigating
823 mechanisms of cellular mechanosensitivity in response to biomechanical strain, and permits
824 systematic future manipulation of ECM components/structure, oxygen availability, and even
825 incorporation of additional cell types to further characterize ONH cell mechanobehavior.
826
827
828
829
830
831
832
833
834
835
836
837
838
839
840
841
842
843
844

845 **Disclosure**

846 The authors report no conflicts of interest.

847

848 **Funding**

849 This project was supported in part by a National Institutes of Health (NIH) grant
850 K08EY031755 (to P.S.G.), R01EY036880 (to P.S.G.), R21EY036198 (to P.S.G.), NIH/National
851 Eye Institute R01EY034096 (to S.H.), R21EY036189 (to S.H.), BrightFocus Foundation
852 G2024006S (to S.H.), David Epstein Career Advancement Award in Glaucoma Research from
853 Research to Prevent Blindness (to S.H.), unrestricted grants from Research to Prevent Blindness
854 and Lions Region 20-Y1 to SUNY Upstate Medical University Department of Ophthalmology and
855 Visual Sciences, R35GM142963 (to A.E.P.), R01EY023242 (to Y.L.), R01EY023242S (to Y.L.),
856 R21EY033961 (to Y.L.), R01EY032960 (to Y.L.), R21EY028671 (to Y.L.), and P30EY031631
857 (to Y.L.), and private foundations, The Glaucoma Foundation, the BrightFocus Foundation, and
858 the Glaucoma Research Foundation, (to Y.L.), R21NS139236 (to M.V.).

859

860 **Acknowledgments**

861 We thank the Neuroscience Microscopy Core at Upstate Medical University and the Blatt
862 BioImaging Center at Syracuse University for imaging support. **Author contributions:** A.N.S.,
863 S.P, M-T. H. T., A.K., S.G., M.P.G., M.V., Y.L., A.E.P., S.H. and P.S.G. designed all experiments,
864 collected, analyzed, and interpreted the data. A.N.S and P.S.G. wrote the manuscript. All authors
865 commented on and approved the final manuscript. S.H. and P.S.G conceived and supervised the
866 research.

867

Data and materials availability: All data needed to evaluate the conclusions in the paper are present in the paper and/or the Supplementary Materials, and RNAsequencing Data available on NIH GEO DataSets GSE300233.. Additional data related to this paper may be requested from the authors.

References

1. Placone AL, Quinones-Hinojosa A, Searson PC: **The role of astrocytes in the progression of brain cancer: complicating the picture of the tumor microenvironment.** *Tumour Biol* 2016, **37:**61-69.
2. Brandao M, Simon T, Critchley G, Giamas G: **Astrocytes, the rising stars of the glioblastoma microenvironment.** *Glia* 2019, **67:**779-790.
3. Gonzalez-Perez O, Lopez-Virgen V, Quinones-Hinojosa A: **Astrocytes: Everything but the glue.** *Neuroimmunol Neuroinflamm* 2015, **2:**115-117.
4. Escartin C, Galea E, Lakatos A, O'Callaghan JP, Petzold GC, Serrano-Pozo A, Steinhauser C, Volterra A, Carmignoto G, Agarwal A, et al: **Reactive astrocyte nomenclature, definitions, and future directions.** *Nat Neurosci* 2021, **24:**312-325.
5. Mishra A, Reynolds JP, Chen Y, Gourine AV, Rusakov DA, Attwell D: **Astrocytes mediate neurovascular signaling to capillary pericytes but not to arterioles.** *Nat Neurosci* 2016, **19:**1619-1627.
6. Verkhratsky A, Nedergaard M: **Physiology of Astroglia.** *Physiol Rev* 2018, **98:**239-389.
7. Turovsky EA, Braga A, Yu Y, Esteras N, Korsak A, Theparambil SM, Hadjihambi A, Hosford PS, Teschemacher AG, Marina N, et al: **Mechanosensory Signaling in Astrocytes.** *J Neurosci* 2020, **40:**9364-9371.
8. Choi HJ, Sun D, Jakobs TC: **Astrocytes in the optic nerve head express putative mechanosensitive channels.** *Mol Vis* 2015, **21:**749-766.
9. Bizanti A, Chandrashekar P, Steward R, Jr.: **Culturing astrocytes on substrates that mimic brain tumors promotes enhanced mechanical forces.** *Exp Cell Res* 2021, **406:**112751.
10. Chekhonin IV, Chistiakov DA, Grinenko NF, Gurina OI: **Glioma Cell and Astrocyte Co-cultures As a Model to Study Tumor-Tissue Interactions: A Review of Methods.** *Cell Mol Neurobiol* 2018, **38:**1179-1195.
11. Hu Y, Huang G, Tian J, Qiu J, Jia Y, Feng D, Wei Z, Li S, Xu F: **Matrix stiffness changes affect astrocyte phenotype in an in vitro injury model.** *NPG Asia Materials* 2021, **13:**35.
12. Ben Haim L, Carrillo-de Sauvage MA, Ceyzeriat K, Escartin C: **Elusive roles for reactive astrocytes in neurodegenerative diseases.** *Front Cell Neurosci* 2015, **9:**278.
13. Garcia-Bermudez MY, Freude KK, Mouhammad ZA, van Wijngaarden P, Martin KK, Kolko M: **Glial Cells in Glaucoma: Friends, Foes, and Potential Therapeutic Targets.** *Front Neurol* 2021, **12:**624983.
14. Albalawi F, Lu W, Beckel JM, Lim JC, McCaughey SA, Mitchell CH: **The P2X7 Receptor Primes IL-1beta and the NLRP3 Inflammasome in Astrocytes Exposed to Mechanical Strain.** *Front Cell Neurosci* 2017, **11:**227.
15. Beckel JM, Argall AJ, Lim JC, Xia J, Lu W, Coffey EE, Macarak EJ, Shahidullah M, Delamere NA, Zode GS, et al: **Mechanosensitive release of adenosine 5'-triphosphate through pannexin channels and mechanosensitive upregulation of pannexin channels in optic nerve head astrocytes: a mechanism for purinergic involvement in chronic strain.** *Glia* 2014, **62:**1486-1501.
16. Weinreb RN, Aung T, Medeiros FA: **The pathophysiology and treatment of glaucoma: a review.** *JAMA* 2014, **311:**1901-1911.

935 17. Nickells RW, Howell GR, Soto I, John SW: **Under pressure: cellular and molecular**
936 **responses during glaucoma, a common neurodegeneration with axonopathy.** *Annu*
937 *Rev Neurosci* 2012, **35:**153-179.
938 18. Tehrani S, Davis L, Cepurna WO, Delf RK, Lozano DC, Choe TE, Johnson EC, Morrison
939 JC: **Optic Nerve Head Astrocytes Display Axon-Dependent and -Independent**
940 **Reactivity in Response to Acutely Elevated Intraocular Pressure.** *Invest Ophthalmol*
941 *Vis Sci* 2019, **60:**312-321.
942 19. Lozano DC, Choe TE, Cepurna WO, Morrison JC, Johnson EC: **Early Optic Nerve Head**
943 **Glial Proliferation and Jak-Stat Pathway Activation in Chronic Experimental**
944 **Glaucoma.** *Invest Ophthalmol Vis Sci* 2019, **60:**921-932.
945 20. Cooper ML, Pasini S, Lambert WS, D'Alessandro KB, Yao V, Risner ML, Calkins DJ:
946 **Redistribution of metabolic resources through astrocyte networks mitigates**
947 **neurodegenerative stress.** *Proc Natl Acad Sci U S A* 2020, **117:**18810-18821.
948 21. Tehrani S, Davis L, Cepurna WO, Choe TE, Lozano DC, Monfared A, Cooper L, Cheng
949 J, Johnson EC, Morrison JC: **Astrocyte Structural and Molecular Response to Elevated**
950 **Intraocular Pressure Occurs Rapidly and Precedes Axonal Tubulin Rearrangement**
951 **within the Optic Nerve Head in a Rat Model.** *PLoS One* 2016, **11:**e0167364.
952 22. Sun D, Lye-Barthel M, Masland RH, Jakobs TC: **Structural remodeling of fibrous**
953 **astrocytes after axonal injury.** *J Neurosci* 2010, **30:**14008-14019.
954 23. Sun D, Moore S, Jakobs TC: **Optic nerve astrocyte reactivity protects function in**
955 **experimental glaucoma and other nerve injuries.** *J Exp Med* 2017, **214:**1411-1430.
956 24. Hernandez MR: **The optic nerve head in glaucoma: role of astrocytes in tissue**
957 **remodeling.** *Prog Retin Eye Res* 2000, **19:**297-321.
958 25. Zode GS, Sethi A, Brun-Zinkernagel AM, Chang IF, Clark AF, Wordinger RJ:
959 **Transforming growth factor-beta2 increases extracellular matrix proteins in optic**
960 **nerve head cells via activation of the Smad signaling pathway.** *Mol Vis* 2011, **17:**1745-
961 1758.
962 26. Pena JD, Taylor AW, Ricard CS, Vidal I, Hernandez MR: **Transforming growth factor**
963 **beta isoforms in human optic nerve heads.** *Br J Ophthalmol* 1999, **83:**209-218.
964 27. Pappenhagen N, Yin E, Morgan AB, Kiehlbauch CC, Inman DM: **Stretch stress propels**
965 **glutamine dependency and glycolysis in optic nerve head astrocytes.** *Front Neurosci*
966 2022, **16:**957034.
967 28. Korneva A, Kimball EC, Quillen S, Jefferys JL, Nawathe M, Ling YTT, Nguyen TD,
968 Quigley HA: **Mechanical strain in the mouse astrocytic lamina increases after**
969 **exposure to recombinant trypsin.** *Acta Biomater* 2023, **163:**312-325.
970 29. Sigal IA, Flanagan JG, Tertinegg I, Ethier CR: **Predicted extension, compression and**
971 **shearing of optic nerve head tissues.** *Exp Eye Res* 2007, **85:**312-322.
972 30. Tamm ER, Ethier CR, Lasker IIoA, Glaucomatous Neurodegeneration P: **Biological**
973 **aspects of axonal damage in glaucoma: A brief review.** *Exp Eye Res* 2017, **157:**5-12.
974 31. Salvador-Silva M, Aoi S, Parker A, Yang P, Pecen P, Hernandez MR: **Responses and**
975 **signaling pathways in human optic nerve head astrocytes exposed to hydrostatic**
976 **pressure in vitro.** *Glia* 2004, **45:**364-377.
977 32. Li Z, Peng F, Liu Z, Li S, Li L, Qian X: **Mechanobiological responses of astrocytes in**
978 **optic nerve head due to biaxial stretch.** *BMC Ophthalmol* 2022, **22:**368.

33. Strat AN, Kirschner A, Yoo H, Singh A, Bague T, Li H, Herberg S, Ganapathy PS: **Engineering a 3D hydrogel system to study optic nerve head astrocyte morphology and behavior.** *Exp Eye Res* 2022, **220:**109102.
34. Mulvihill JJE, Raykin J, Snider EJ, Schildmeyer LA, Zaman I, Platt MO, Kelly DJ, Ethier CR: **Development of a Platform for Studying 3D Astrocyte Mechanobiology: Compression of Astrocytes in Collagen Gels.** *Ann Biomed Eng* 2018, **46:**365-374.
35. Thorpe SD, Nagel T, Carroll SF, Kelly DJ: **Modulating gradients in regulatory signals within mesenchymal stem cell seeded hydrogels: a novel strategy to engineer zonal articular cartilage.** *PLoS One* 2013, **8:**e60764.
36. McDermott AM, Herberg S, Mason DE, Collins JM, Pearson HB, Dawahare JH, Tang R, Patwa AN, Grinstaff MW, Kelly DJ, et al: **Recapitulating bone development through engineered mesenchymal condensations and mechanical cues for tissue regeneration.** *Sci Transl Med* 2019, **11**.
37. Kirschner A, Strat AN, Yablonski J, Yoo H, Bague T, Li H, Zhao J, Bollinger KE, Herberg S, Ganapathy PS: **Mechanosensitive channel inhibition attenuates TGFbeta2-induced actin cytoskeletal remodeling and reactivity in mouse optic nerve head astrocytes.** *Exp Eye Res* 2021, **212:**108791.
38. Ho Thanh MT, Poudel A, Ameen S, Carroll B, Wu M, Soman P, Zhang T, Schwarz JM, Patteson AE: **Vimentin promotes collective cell migration through collagen networks via increased matrix remodeling and spheroid fluidity.** *bioRxiv* 2024.
39. Stein AM, Vader DA, Jawerth LM, Weitz DA, Sander LM: **An algorithm for extracting the network geometry of three-dimensional collagen gels.** *J Microsc* 2008, **232:**463-475.
40. Munster S, Fabry B: **A simplified implementation of the bubble analysis of biopolymer network pores.** *Biophys J* 2013, **104:**2774-2775.
41. Adeoye AJ, de Alba E: **A Simple Method to Determine Diffusion Coefficients in Soft Hydrogels for Drug Delivery and Biomedical Applications.** *ACS Omega* 2025, **10:**10852-10865.
42. Lepsky VR, Natan S, Tchaicheeyan O, Kolel A, Zussman M, Zilberman M, Lesman A: **FITC-Dextran Release from Cell-Embedded Fibrin Hydrogels.** *Biomolecules* 2021, **11**.
43. Coelho NM, Wang A, Petrovic P, Wang Y, Lee W, McCulloch CA: **MRIP Regulates the Myosin IIA Activity and DDR1 Function to Enable Collagen Tractional Remodeling.** *Cells* 2020, **9**.
44. Sullivan GM, Feinn R: **Using Effect Size-or Why the P Value Is Not Enough.** *J Grad Med Educ* 2012, **4:**279-282.
45. Elizarraras JM, Liao Y, Shi Z, Zhu Q, Pico AR, Zhang B: **WebGestalt 2024: faster gene set analysis and new support for metabolomics and multi-omics.** *Nucleic Acids Res* 2024, **52:**W415-W421.
46. Wang J, Duncan D, Shi Z, Zhang B: **WEB-based GEne SeT AnaLysis Toolkit (WebGestalt): update 2013.** *Nucleic Acids Res* 2013, **41:**W77-83.
47. Rust R, Kirabali T, Gronnert L, Dogancay B, Limasale YDP, Meinhardt A, Werner C, Lavina B, Kulic L, Nitsch RM, et al: **A Practical Guide to the Automated Analysis of Vascular Growth, Maturation and Injury in the Brain.** *Front Neurosci* 2020, **14:**244.
48. Nichols AJ, O'Dell RS, Powrozek TA, Olson EC: **Ex utero electroporation and whole hemisphere explants: a simple experimental method for studies of early cortical development.** *J Vis Exp* 2013.

1025 49. Li, Bague T, Kirschner A, Strat AN, Roberts H, Weisenthal RW, Patteson AE, Annabi N,
1026 Stamer WD, Ganapathy PS, Herberg S: **A tissue-engineered human trabecular**
1027 **meshwork hydrogel for advanced glaucoma disease modeling.** *Exp Eye Res* 2021,
1028 **205:**108472.
1029 50. Sun D, Lye-Barthel M, Masland RH, Jakobs TC: **The morphology and spatial**
1030 **arrangement of astrocytes in the optic nerve head of the mouse.** *J Comp Neurol* 2009,
1031 **516:**1-19.
1032 51. Lye-Barthel M, Sun D, Jakobs TC: **Morphology of astrocytes in a glaucomatous optic**
1033 **nerve.** *Invest Ophthalmol Vis Sci* 2013, **54:**909-917.
1034 52. Tu C, Fiandalo MV, Pop E, Stocking JJ, Azabdaftari G, Li J, Wei H, Ma D, Qu J, Mohler
1035 JL, et al: **Proteomic Analysis of Charcoal-Stripped Fetal Bovine Serum Reveals**
1036 **Changes in the Insulin-like Growth Factor Signaling Pathway.** *J Proteome Res* 2018,
1037 **17:**2963-2977.
1038 53. Yildiz A, Kara AA, Acarturk F: **Peptide-protein based nanofibers in pharmaceutical**
1039 **and biomedical applications.** *Int J Biol Macromol* 2020, **148:**1084-1097.
1040 54. Harris RC, Chung E, Coffey RJ: **EGF receptor ligands.** *Exp Cell Res* 2003, **284:**2-13.
1041 55. Mazumder AG, Jule AM, Sun D: **Astrocytes of the optic nerve exhibit a region-specific**
1042 **and temporally distinct response to elevated intraocular pressure.** *Mol Neurodegener*
1043 2023, **18:**68.
1044 56. Johnson EC, Jia L, Cepurna WO, Doser TA, Morrison JC: **Global changes in optic nerve**
1045 **head gene expression after exposure to elevated intraocular pressure in a rat**
1046 **glaucoma model.** *Invest Ophthalmol Vis Sci* 2007, **48:**3161-3177.
1047 57. Pitha I, Du L, Nguyen TD, Quigley H: **IOP and glaucoma damage: The essential role**
1048 **of optic nerve head and retinal mechanosensors.** *Prog Retin Eye Res* 2024, **99:**101232.
1049 58. Hernandez MR, Miao H, Lukas T: **Astrocytes in glaucomatous optic neuropathy.** *Prog*
1050 *Brain Res* 2008, **173:**353-373.
1051 59. Nsiah NY, Morgan AB, Donkor N, Inman DM: **Long-term HIF-1alpha stabilization**
1052 **reduces respiration, promotes mitophagy, and results in retinal cell death.** *Sci Rep*
1053 2023, **13:**20541.
1054 60. Jassim AH, Fan Y, Pappenhagen N, Nsiah NY, Inman DM: **Oxidative Stress and Hypoxia**
1055 **Modify Mitochondrial Homeostasis During Glaucoma.** *Antioxid Redox Signal* 2021,
1056 **35:**1341-1357.
1057 61. Jassim AH, Nsiah NY, Inman DM: **Ocular Hypertension Results in Hypoxia within Glia**
1058 **and Neurons throughout the Visual Projection.** *Antioxidants (Basel)* 2022, **11**.
1059 62. Hernandez MR, Andrzejewska WM, Neufeld AH: **Changes in the extracellular matrix**
1060 **of the human optic nerve head in primary open-angle glaucoma.** *Am J Ophthalmol*
1061 1990, **109:**180-188.
1062 63. Hernandez MR, Ye H: **Glaucoma: changes in extracellular matrix in the optic nerve**
1063 **head.** *Ann Med* 1993, **25:**309-315.
1064 64. Geiduschek EK, McDowell CM: **The Fibro-Inflammatory Response in the**
1065 **Glaucomatous Optic Nerve Head.** *Int J Mol Sci* 2023, **24**.
1066 65. Schneider M, Fuchshofer R: **The role of astrocytes in optic nerve head fibrosis in**
1067 **glaucoma.** *Exp Eye Res* 2016, **142:**49-55.
1068 66. Krishna V, Andrews H, Jin X, Yu J, Varma A, Wen X, Kindy M: **A contusion model of**
1069 **severe spinal cord injury in rats.** *J Vis Exp* 2013.

1070 67. Shields J, Kimbler DE, Radwan W, Yanasak N, Sukumari-Ramesh S, Dhandapani KM:
1071 **Therapeutic targeting of astrocytes after traumatic brain injury.** *Transl Stroke Res*
1072 2011, **2:**633-642.
1073 68. Wei R, Zhou J, Bui B, Liu X: **Glioma actively orchestrate a self-advantageous**
1074 **extracellular matrix to promote recurrence and progression.** *BMC Cancer* 2024,
1075 **24:**974.
1076 69. Ricard CS, Kobayashi S, Pena JD, Salvador-Silva M, Agapova O, Hernandez MR:
1077 **Selective expression of neural cell adhesion molecule (NCAM)-180 in optic nerve head**
1078 **astrocytes exposed to elevated hydrostatic pressure in vitro.** *Brain Res Mol Brain Res*
1079 2000, **81:**62-79.
1080 70. Caliari SR, Burdick JA: **A practical guide to hydrogels for cell culture.** *Nat Methods*
1081 2016, **13:**405-414.
1082 71. Vallejo-Giraldo C, Genta M, Cauvi O, Goding J, Green R: **Hydrogels for 3D Neural**
1083 **Tissue Models: Understanding Cell-Material Interactions at a Molecular Level.** *Front*
1084 *Bioeng Biotechnol* 2020, **8:**601704.
1085 72. Park S, Park KM: **Engineered Polymeric Hydrogels for 3D Tissue Models.** *Polymers*
1086 *(Basel)* 2016, **8**.
1087 73. Son JL, Soto I, Oglesby E, Lopez-Roca T, Pease ME, Quigley HA, Marsh-Armstrong N:
1088 **Glaucomatous optic nerve injury involves early astrocyte reactivity and late**
1089 **oligodendrocyte loss.** *Glia* 2010, **58:**780-789.
1090 74. Quillen S, Schaub J, Quigley H, Pease M, Korneva A, Kimball E: **Astrocyte responses to**
1091 **experimental glaucoma in mouse optic nerve head.** *PLoS One* 2020, **15:**e0238104.
1092 75. Balaratnasingam C, Morgan WH, Bass L, Ye L, McKnight C, Cringle SJ, Yu DY:
1093 **Elevated pressure induced astrocyte damage in the optic nerve.** *Brain Res* 2008,
1094 **1244:**142-154.
1095 76. Lu W, Albalawi F, Beckel JM, Lim JC, Laties AM, Mitchell CH: **The P2X7 receptor**
1096 **links mechanical strain to cytokine IL-6 up-regulation and release in neurons and**
1097 **astrocytes.** *J Neurochem* 2017, **141:**436-448.
1098 77. Furukawa R, Maselli A, Thomson SA, Lim RW, Stokes JV, Fechheimer M: **Calcium**
1099 **regulation of actin crosslinking is important for function of the actin cytoskeleton in**
1100 **Dictyostelium.** *J Cell Sci* 2003, **116:**187-196.
1101 78. Sergeeva M, Ubl JJ, Reiser G: **Disruption of actin cytoskeleton in cultured rat**
1102 **astrocytes suppresses ATP- and bradykinin-induced [Ca(2+)](i) oscillations by**
1103 **reducing the coupling efficiency between Ca(2+) release, capacitative Ca(2+) entry,**
1104 **and store refilling.** *Neuroscience* 2000, **97:**765-769.
1105 79. Kamel K, O'Brien CJ, Zhdanov AV, Papkovsky DB, Clark AF, Stamer WD, Irnaten M:
1106 **Reduced Oxidative Phosphorylation and Increased Glycolysis in Human Glaucoma**
1107 **Lamina Cribrosa Cells.** *Invest Ophthalmol Vis Sci* 2020, **61:**4.
1108 80. Kirwan RP, Felice L, Clark AF, O'Brien CJ, Leonard MO: **Hypoxia regulated gene**
1109 **transcription in human optic nerve lamina cribrosa cells in culture.** *Invest Ophthalmol*
1110 *Vis Sci* 2012, **53:**2243-2255.
1111 81. Mylonis I, Simos G, Paraskeva E: **Hypoxia-Inducible Factors and the Regulation of**
1112 **Lipid Metabolism.** *Cells* 2019, **8**.
1113 82. Green DR, Galluzzi L, Kroemer G: **Cell biology. Metabolic control of cell death.** *Science*
1114 2014, **345:**1250256.

1115 83. Inman DM, Harun-Or-Rashid M: **Metabolic Vulnerability in the Neurodegenerative**
1116 **Disease Glaucoma.** *Front Neurosci* 2017, **11:**146.
1117 84. Islam MR, Ji F, Bansal M, Hua Y, Sigal IA: **Fibrous finite element modeling of the optic**
1118 **nerve head region.** *Acta Biomater* 2024, **175:**123-137.
1119 85. Howell GR, Libby RT, Jakobs TC, Smith RS, Phalan FC, Barter JW, Barbay JM, Marchant
1120 JK, Mahesh N, Porciatti V, et al: **Axons of retinal ganglion cells are insulted in the optic**
1121 **nerve early in DBA/2J glaucoma.** *J Cell Biol* 2007, **179:**1523-1537.
1122 86. Korneva A, Kimball EC, Johnson TV, Quillen SE, Pease ME, Quigley HA, Nguyen TD:
1123 **Comparison of the Biomechanics of the Mouse Astrocytic Lamina Cribrosa Between**
1124 **Glaucoma and Optic Nerve Crush Models.** *Invest Ophthalmol Vis Sci* 2023, **64:**14.
1125 87. Alarcon-Martinez L, Villafranca-Baughman D, Quintero H, Kacerovsky JB, Dotigny F,
1126 Murai KK, Prat A, Drapeau P, Di Polo A: **Interpericyte tunnelling nanotubes regulate**
1127 **neurovascular coupling.** *Nature* 2020, **585:**91-95.
1128 88. Morrison JC, Cepurna Ying Guo WO, Johnson EC: **Pathophysiology of human**
1129 **glaucomatous optic nerve damage: insights from rodent models of glaucoma.** *Exp Eye*
1130 *Res* 2011, **93:**156-164.
1131 89. Pang IH, Clark AF: **Rodent models for glaucoma retinopathy and optic neuropathy.** *J*
1132 *Glaucoma* 2007, **16:**483-505.
1133 90. Placone AL, McGuiggan PM, Bergles DE, Guerrero-Cazares H, Quinones-Hinojosa A,
1134 Searson PC: **Human astrocytes develop physiological morphology and remain**
1135 **quiescent in a novel 3D matrix.** *Biomaterials* 2015, **42:**134-143.
1136 91. Duan B, Hockaday LA, Kapetanovic E, Kang KH, Butcher JT: **Stiffness and adhesivity**
1137 **control aortic valve interstitial cell behavior within hyaluronic acid based hydrogels.**
1138 *Acta Biomater* 2013, **9:**7640-7650.
1139 92. Lawyer T, McIntosh K, Clavijo C, Potekhina L, Mann BK: **Formulation Changes Affect**
1140 **Material Properties and Cell Behavior in HA-Based Hydrogels.** *Int J Cell Biol* 2012,
1141 **2012:**737421.
1142 93. Rocha DN, Ferraz-Nogueira JP, Barrias CC, Relvas JB, Pego AP: **Extracellular**
1143 **environment contribution to astrogliosis-lessons learned from a tissue engineered 3D**
1144 **model of the glial scar.** *Front Cell Neurosci* 2015, **9:**377.
1145 94. Strat AN, Patel S, Venkatesan A, Carroll R, Chin C, Tso D, Bernstein AM, Herberg S,
1146 Ganapathy PS: **The role of mechanosensitive channels in cellular/metabolic response**
1147 **of optic nerve head (ONH) astrocytes to tension in a 3D hydrogel system.** *Investigative*
1148 *Ophthalmology & Visual Science* 2024, **65:**1201-1201.
1149 95. Strat AN, Kirschner A, Singh A, Sako K, Geiss M, Herberg S, Ganapathy PS: **Optic nerve**
1150 **head astrocyte response to compressive/tensile strains using a 3D hydrogel system.**
1151 *Investigative Ophthalmology & Visual Science* 2023, **64:**4364-4364.
1152

1153

1154

1155

1156

1157 **Supplementary Information**

1158

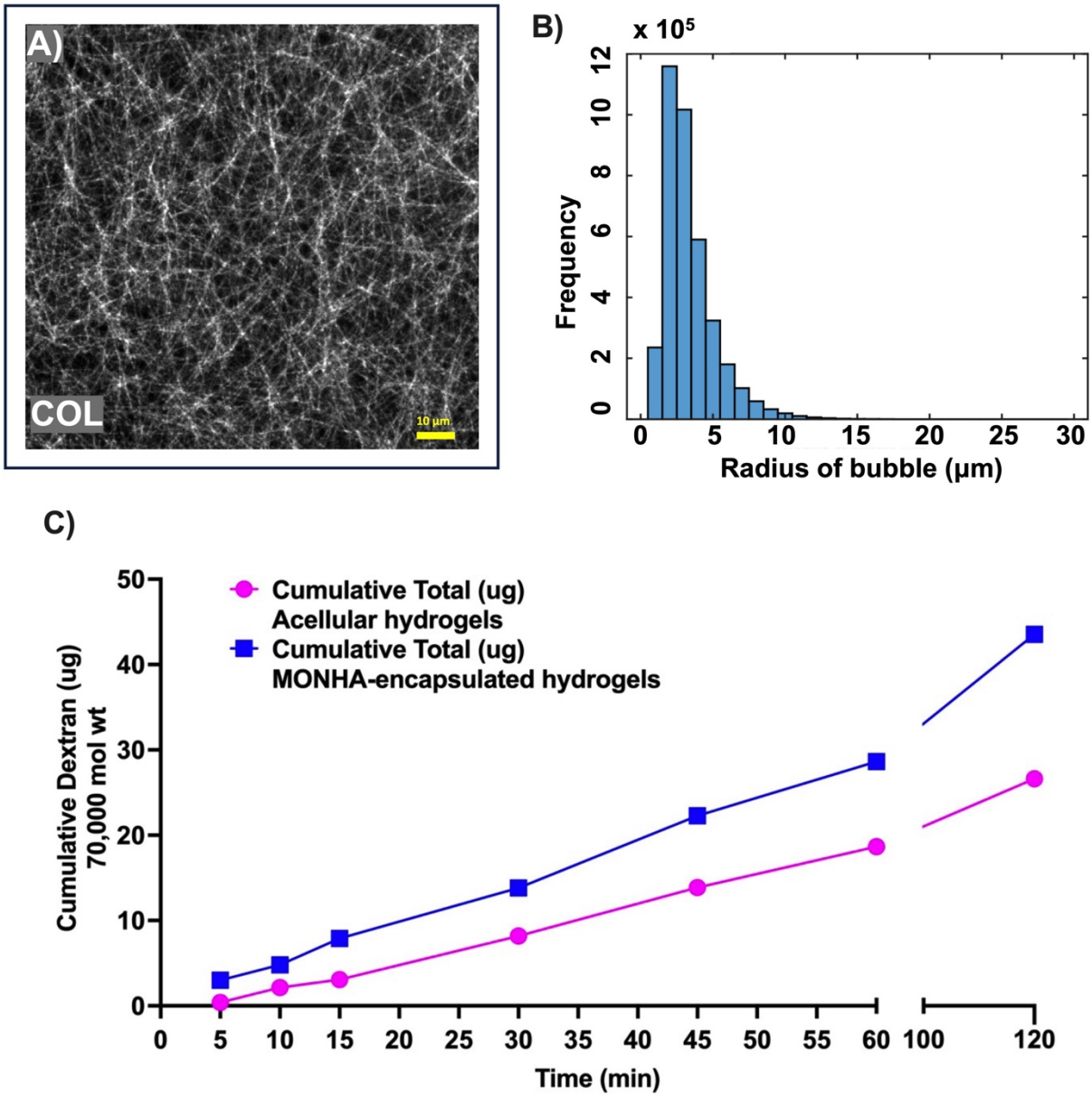

1159

1160 **Supplemental Fig. 1. Characterization of the MONHA-encapsulated hydrogel model system.**
1161 **(A)** Representative fluorescence image of collagen fibril distribution and quantification of pore
1162 size range **(B)** within acellular hydrogels (N = 5). Scale bar 10 µm. **(C)** Assessment of the
1163 normalized average permeability of acellular and MONHA-encapsulated hydrogels (N = 3/group)
1164 as calculated by FITC-labelled 70kDa dextran as tracer molecule.
1165

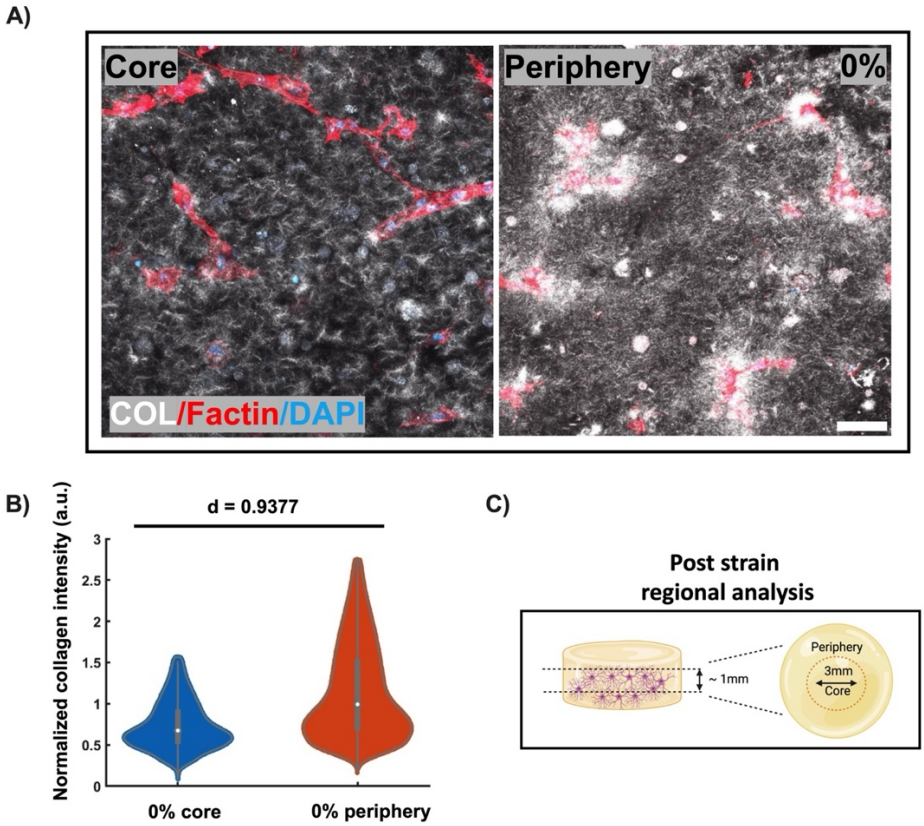

Supplemental Fig. 2. Regional differences in collagen fibril compaction of MONHA-encapsulated hydrogels. (A) Density of collagen fibrils in the core and periphery of the MONHA-encapsulated hydrogels after 2 weeks in culture; scale bar 20 µm. **(B)** Quantitative analysis of normalized collagen compaction within the core and periphery of MONHA-encapsulated hydrogels (N = 3/group). Cohen's d = 0.20, 0.50, and 0.80 is used to indicate the effect sizes as small, medium, or large, respectively. **(C)** Schematic delineating regional segmentation of MONHA-encapsulated hydrogels post biomechanical strain.

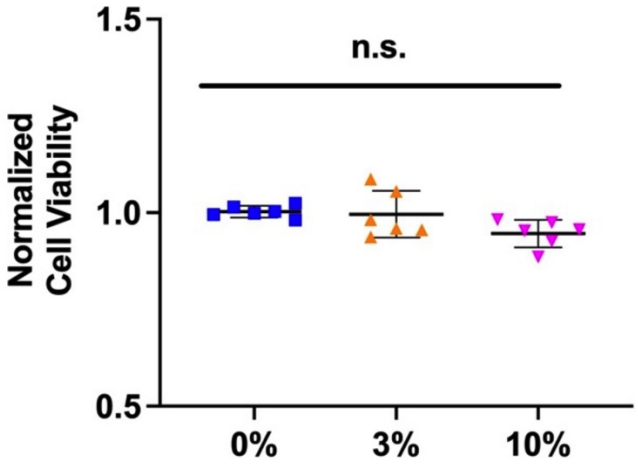

1176 **Supplemental Fig. 3. Cell viability following biomechanical strain.** Normalized MONHA cell
1177 viability after 24h biomechanical strain via MTS assay (N = 6/group). Significance was determined
1178 by one-way ANOVA using multiple comparisons tests.
1179

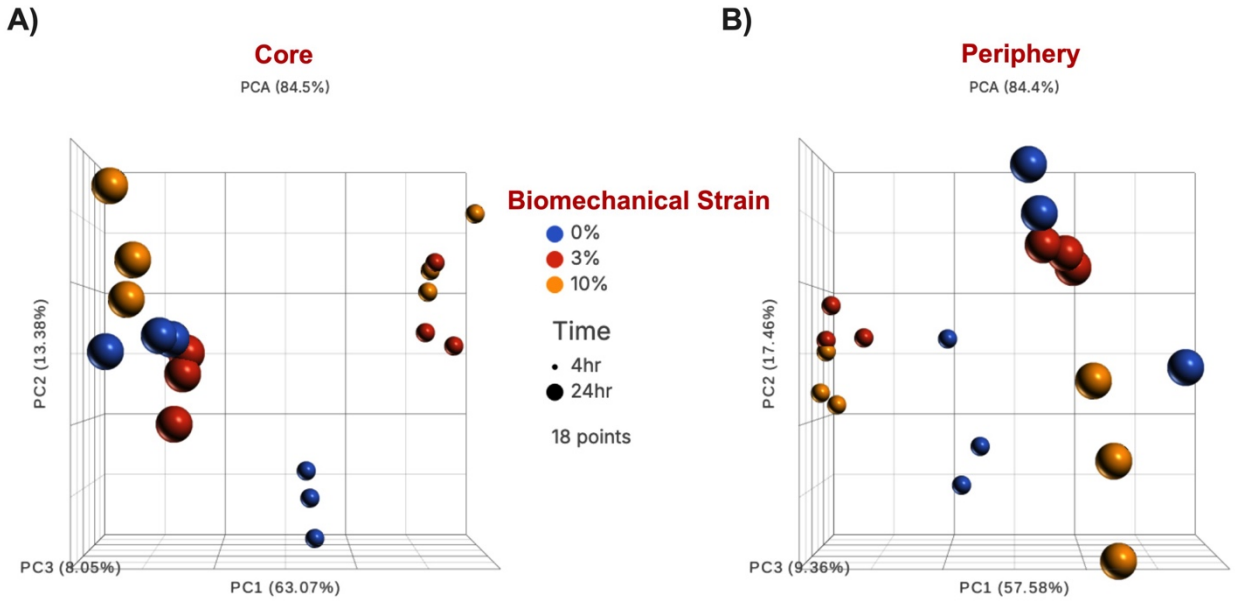

1180

1181 **Supplemental Fig. 4. Regional principal component analyses of encapsulated MONHAs**
1182 **transcriptomes in response to biomechanical strain over time.** Each point represents an
1183 individual replicate per region (n = 18/core and 18/periphery) subjected to cyclic biomechanical
1184 strain (blue = 0%, red = 3%, orange = 10%) for 4 hours (small spheres) or 24 hours (large spheres).
1185 Duration of strain (i.e., time) is the dominant source of variation, with point separation along PC1,
1186 and magnitudes of strain are observed with PC2 and PC3. **(A)** In the core region, the three principal
1187 components (i.e., PC1: 63.07%, PC2: 13.38%, PC3: 8.05%) collectively explain 84.5% of the total
1188 variance. **(B)** In the periphery, the three principal components (i.e., PC1: 57.58%, PC2: 17.46%,
1189 PC3: 9.36%) account for 84.4% of total variance.
1190

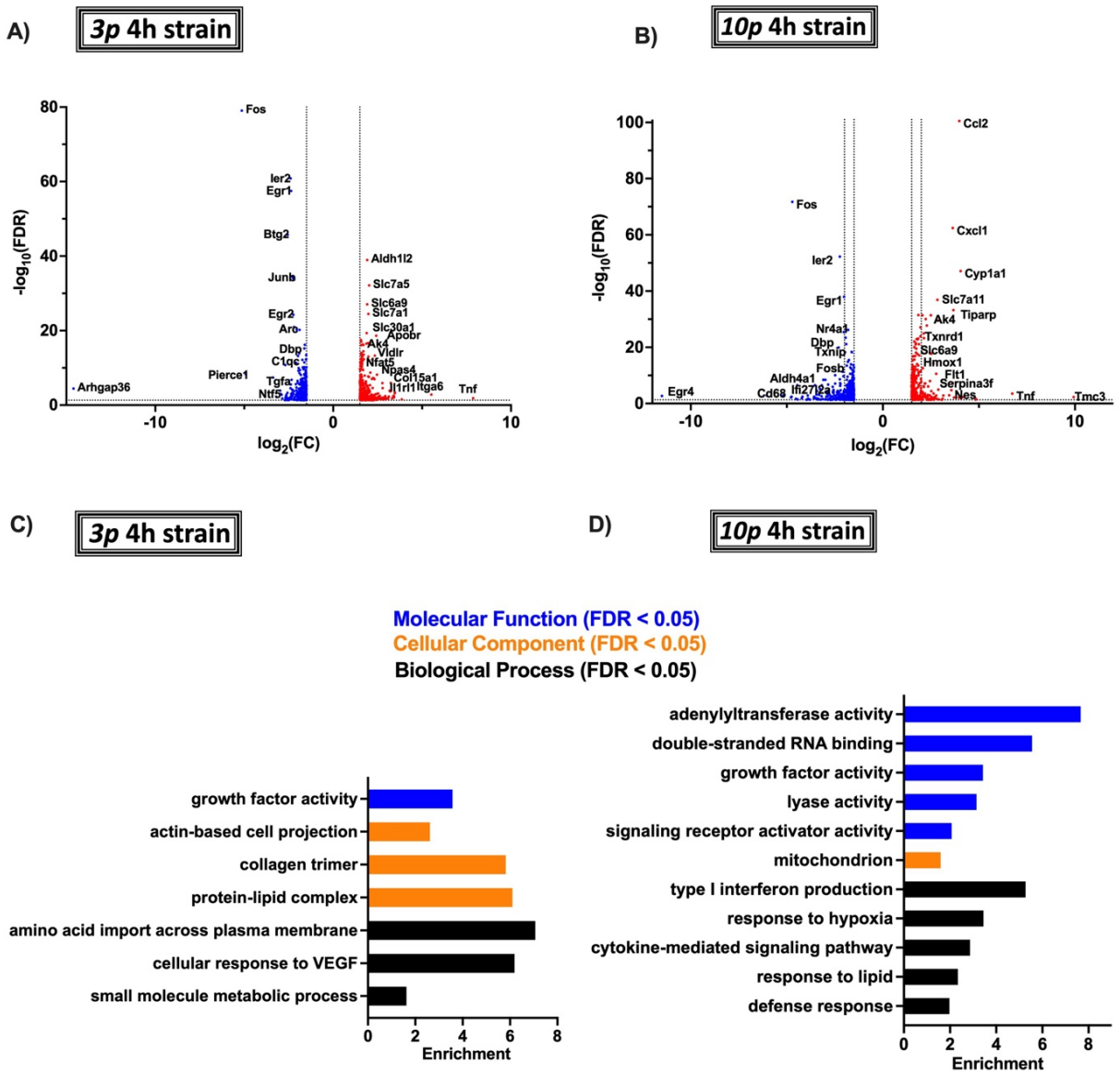

Supplemental Fig. 5. Pairwise transcriptional mechanoresponse of MONHAs encapsulated within the hydrogel periphery to 4h of biomechanical strain. (A-B) Volcano plots representing the number of DEGs with FDR ≤ 0.05 and |FC| ≥ 1.5 in response to 3% and 10% biomechanical strain for 24h. **(C)** Listed are five representative gene ontology (GO) pathways per functional group of the top 30 most significant GOs after 4h of strain.

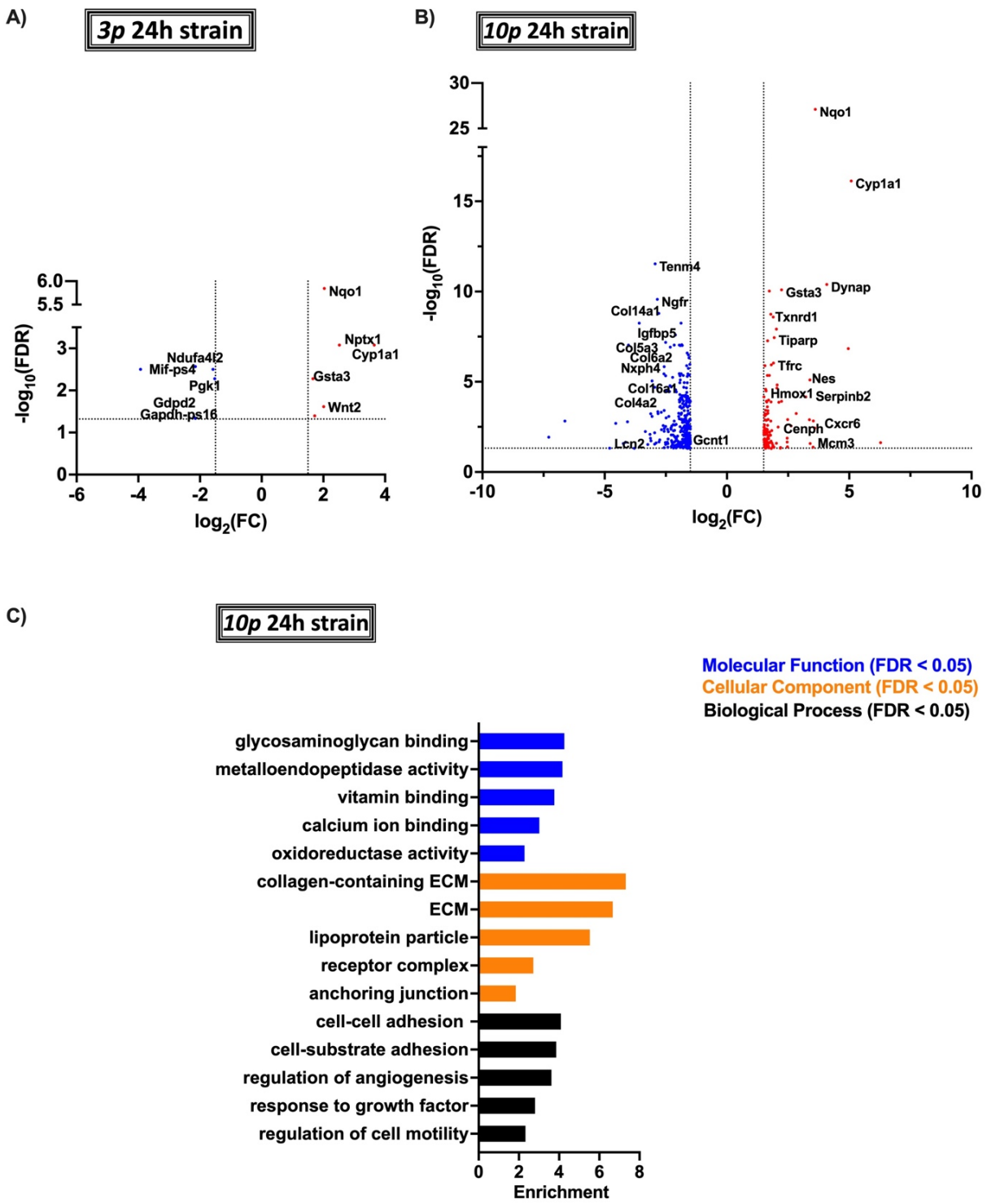

Supplemental Fig. 6. Pairwise transcriptional mechanoresponse of MONHAs encapsulated within the hydrogel periphery to 24h of biomechanical strain. (A-B) Volcano plots representing the number of DEGs for 24h with FDR ≤ 0.05 and |FC| ≥ 1.5 in response to 3% and 10% biomechanical strain for 24h. **(C)** Listed are five representative gene ontology (GO) pathways per functional group of the top 30 most significant GOs at each timepoint.

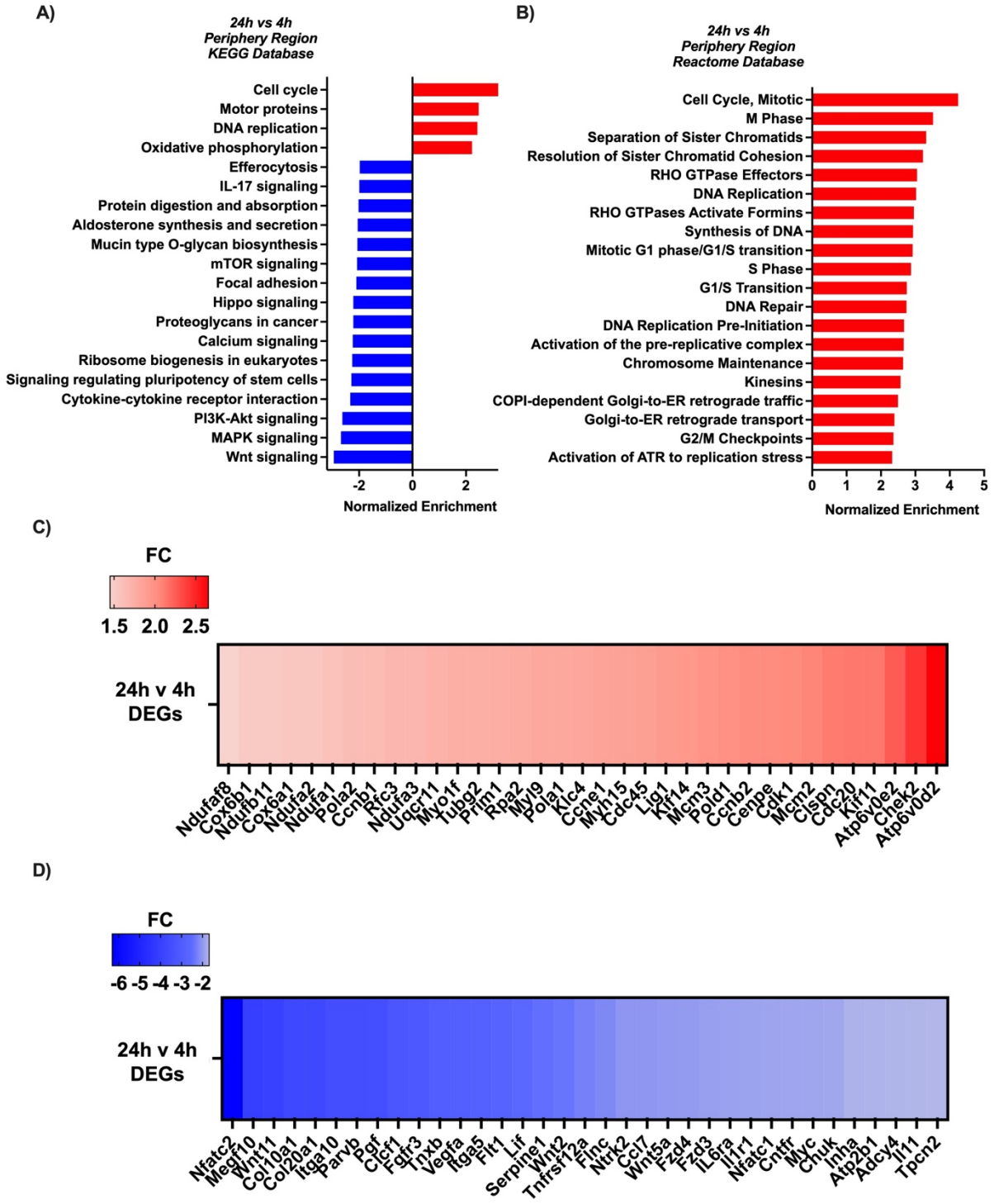

Supplemental Fig. 7. Transcriptional mechanoresponse of MONHAs encapsulated within the hydrogel periphery over time with increasing strain. (A-B) Listed here are 20 up and down most significant pathways against KEGG and Reactome databases with representative 35 DEGs for the **(C)** upregulated and **(D)** downregulated pathways (FDR ≤ 0.05 and |FC| ≥ 1.5)

1209 based on ANOVA analysis of MONHAs mechanoresponse over time (i.e., 24h vs 4h) with
1210 increasing strain.

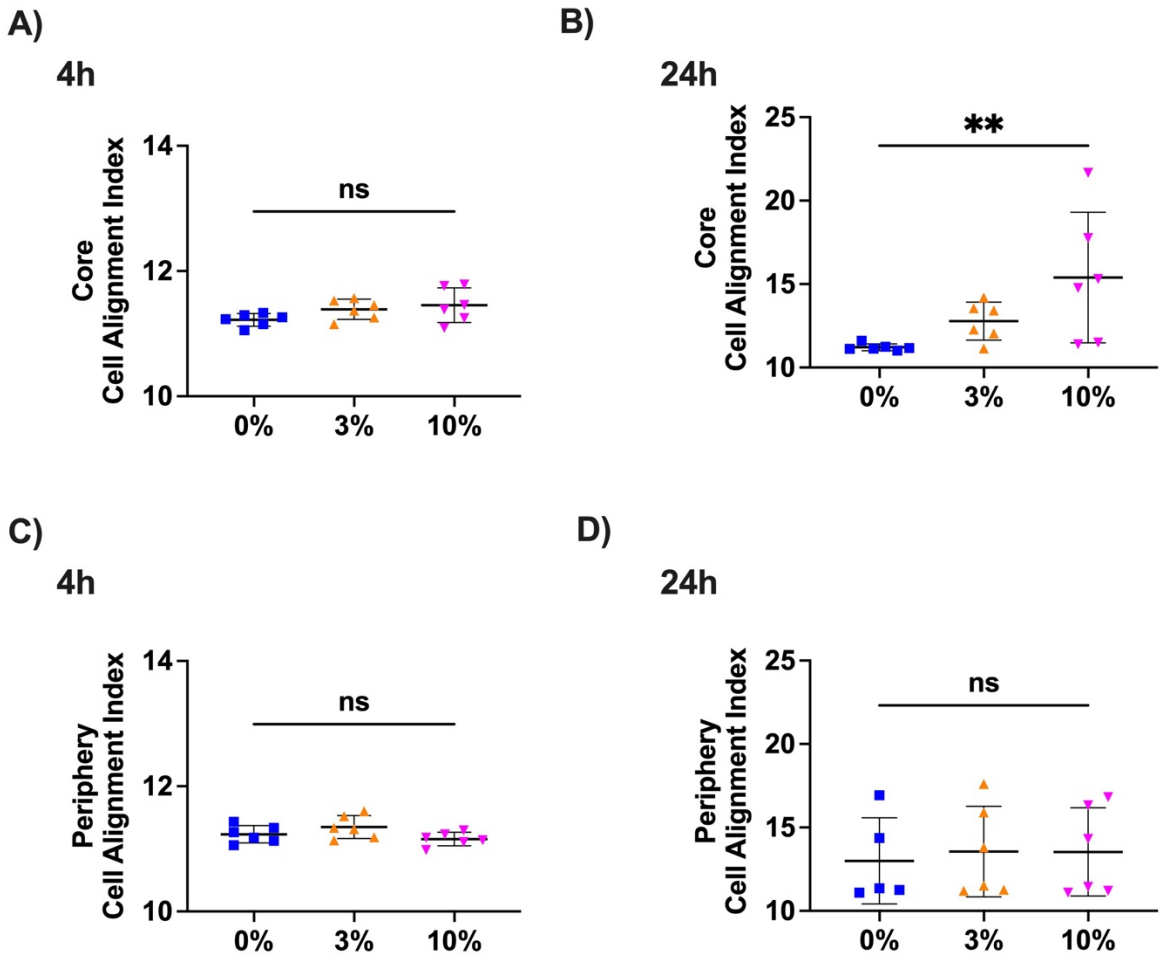

1211
1212
1213 **Supplemental Fig. 8. Regional differences in encapsulated MONHA cell alignment in**
1214 **response to biomechanical strain.** Quantitative analyses of cell alignment based on F-actin mask
1215 area (N = 6 fields of view/group) in response to 4h **(A)** and 24h of increasing biomechanical strain
1216 (i.e., 3% or 10%) **(B)** within the core of the hydrogel, and 4h **(C)** and 24h of biomechanical strain
1217 **(D)** within the periphery of the hydrogel, Statistical significance was determined using one-way
1218 ANOVA (** $p < 0.01$).
1219

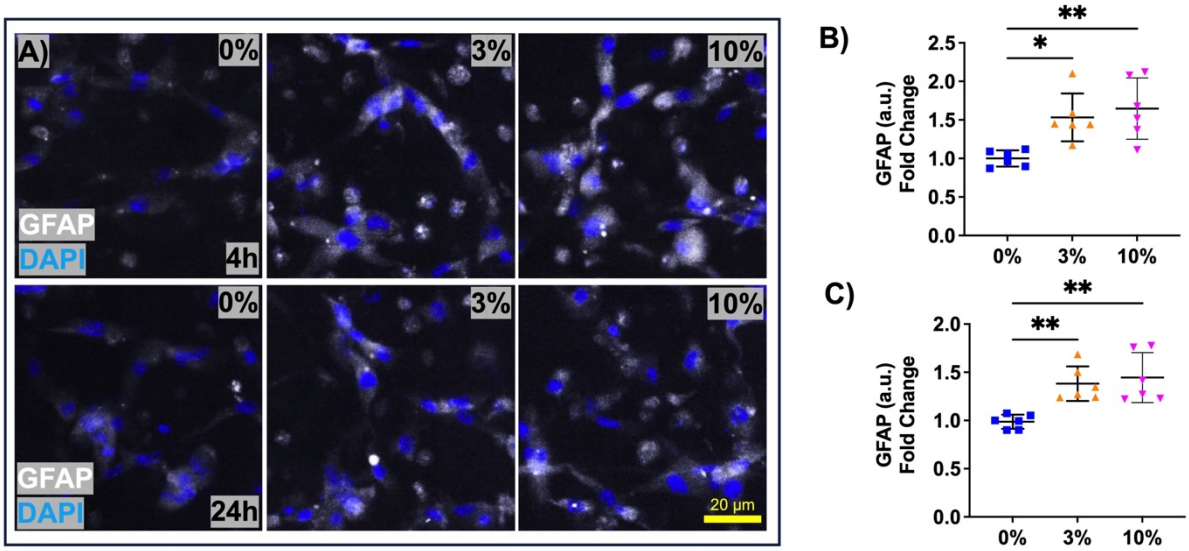

Supplemental Fig. 9. GFAP expression of encapsulated-MONHAs within the hydrogel periphery in response to biomechanical strain. (A) Representative fluorescence images and quantification of fold change in astrocyte GFAP signal intensity (N = 6 fields of view/group) after 4h **(B)** and 24h **(C)** of increasing strain (i.e., 3% or 10%). Statistical significance was determined using one-way ANOVA (*$p < 0.05$, **$p < 0.01$) for GFAP expression levels. Scale bar: 20 µm.

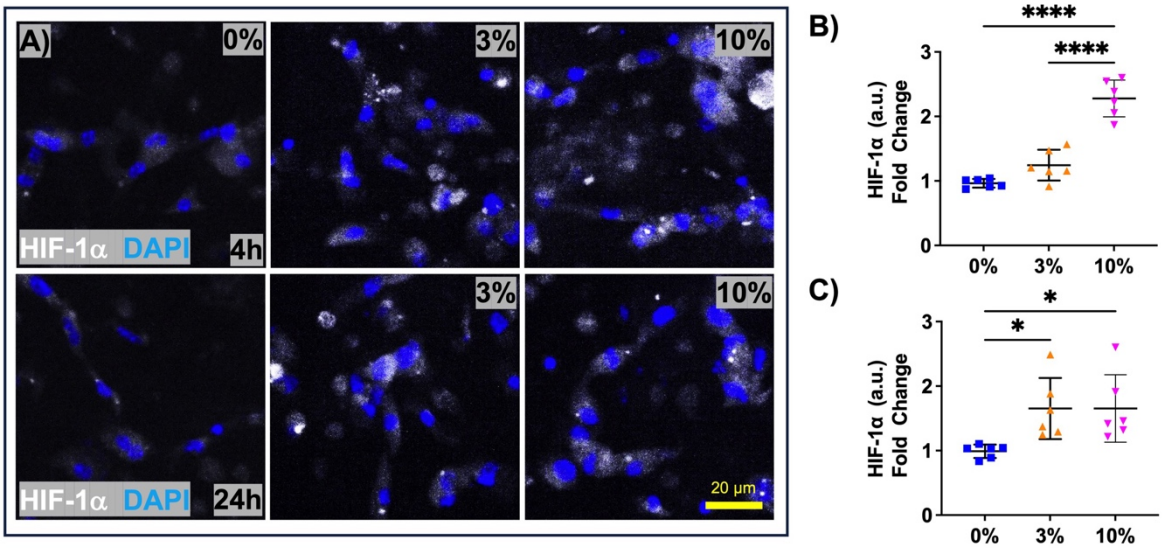

Supplemental Fig. 10. HIF-1α expression of encapsulated-MONHAs within the hydrogel periphery in response to biomechanical strain. (A) Representative fluorescence images and quantification of fold change in astrocyte HIF-1α expression signal intensity (N = 6 fields of view/group) after 4h **(B)** and 24h **(C)** of increasing strain (i.e., 3% or 10%). Statistical significance was determined using one-way ANOVA (*$p < 0.05$, **** $p < 0.0001$) for HIF-1α expression levels. Scale bar: 20 µm.

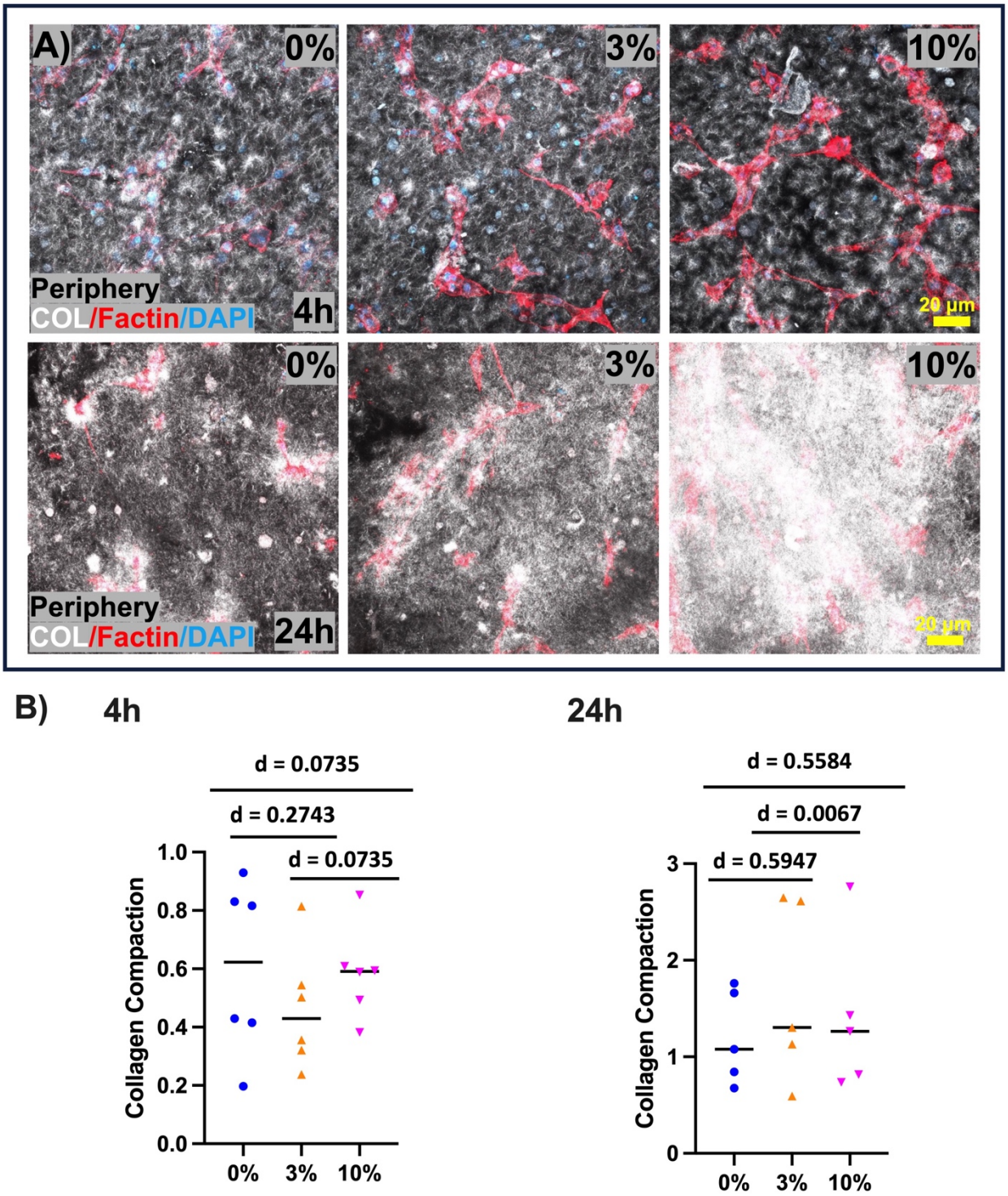

Supplemental Fig. 11. ECM collagen fibrils remodeling in the periphery of MONHA-encapsulated hydrogels in response to biomechanical strain. (A) Representative fluorescence images of collagen fibrils remodeling in response to duration (i.e., 4h or 24h) and magnitude of strain (i.e., 3% or 10%) (N = 6 fields of view/group). Scale bar: 20 µm. **(B)** Quantification of

collagen compaction post strain. Cohen's effect size d (Cohen's d = 0.20, 0.50, and 0.80 is used to indicate the effect sizes as small, medium, or large, respectively).

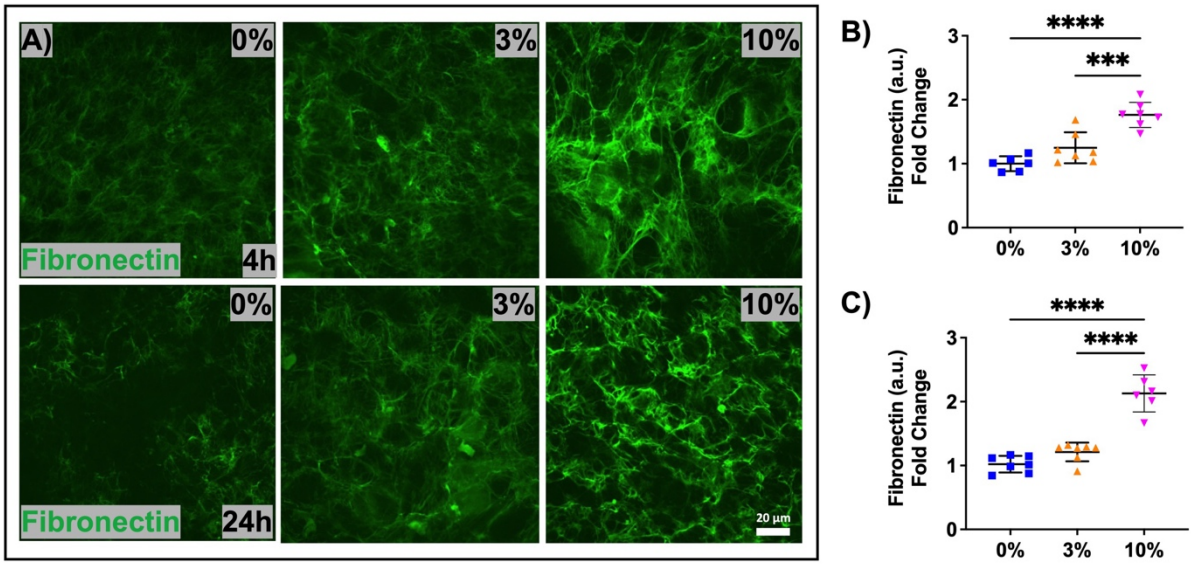

Supplemental Fig. 12. ECM fibronectin secretion in the periphery of MONHA-encapsulated hydrogels in response to biomechanical strain. (A) Representative fluorescence images of fibronectin in response to duration (i.e., 4h or 24h) and magnitude of strain (i.e., 3% or 10%) (N = 6 fields of view/group) and **(B-C)** quantification of fold change in fibronectin signal intensity. Statistical significance was determined using one-way ANOVA (***$p < 0.001$, **** $p < 0.0001$) for fibronectin signal intensity. Scale bar: 20 µm.

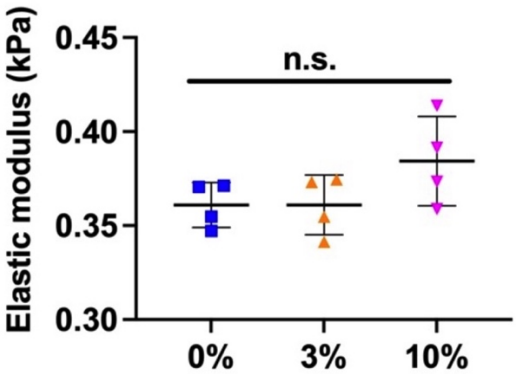

Supplemental Fig. 13. MONHA-encapsulated hydrogel stiffness following biomechanical strain. Analysis of the elastic modulus (kPa) of MONHA-encapsulated hydrogels (N = 4/group) following 24h of increasing biomechanical strain (i.e., 3% or 10%). Significance was determined by one-way ANOVA using multiple comparisons test.